

## STAR FORMATION AROUND MID-INFRARED BUBBLE N37: EVIDENCE OF CLOUD-CLOUD COLLISION

T. BAUG

Department of Astronomy and Astrophysics, Tata Institute of Fundamental Research, Homi Bhabha Road, Mumbai-400005, India

L.K. DEWANGAN

Physical Research Laboratory, Navrangpura, Ahmedabad - 380 009, India.

D.K. OJHA

Department of Astronomy and Astrophysics, Tata Institute of Fundamental Research, Homi Bhabha Road, Mumbai-400005, India

AND

J.P. NINAN

Department of Astronomy and Astrophysics, Tata Institute of Fundamental Research, Homi Bhabha Road, Mumbai-400005, India

## ABSTRACT

We have performed a multi-wavelength analysis of a mid-infrared (MIR) bubble N37 and its surrounding environment. The selected  $15' \times 15'$  area around the bubble contains two molecular clouds (N37 cloud;  $V_{lsr} \sim 37\text{--}43 \text{ km s}^{-1}$ , and C25.29+0.31;  $V_{lsr} \sim 43\text{--}48 \text{ km s}^{-1}$ ) along the line of sight. A total of seven OB stars are identified towards the bubble N37 using photometric criteria, and two of them are spectroscopically confirmed as O9V and B0V stars. Spectro-photometric distances of these two sources confirm their physical association with the bubble. The O9V star is appeared to be the primary ionizing source of the region, which is also in agreement with the desired Lyman continuum flux analysis estimated from the 20 cm data. The presence of the expanding HII region is revealed in the N37 cloud which could be responsible for the MIR bubble. Using the  $^{13}\text{CO}$  line data and photometric data, several cold molecular condensations as well as clusters of young stellar objects (YSOs) are identified in the N37 cloud, revealing ongoing star formation (SF) activities. However, the analysis of ages of YSOs and the dynamical age of the HII region do not support the origin of SF due to the influence of OB stars. The position-velocity analysis of  $^{13}\text{CO}$  data reveals that two molecular clouds are inter-connected by a bridge-like structure, favoring the onset of a cloud-cloud collision process. The SF activities (i.e. the formation of YSOs clusters and OB stars) in the N37 cloud are possibly influenced by the cloud-cloud collision.

*Subject headings:* dust, extinction – H II regions – ISM: clouds – ISM: individual objects (N37) – stars: formation – stars: pre-main sequence

## 1. INTRODUCTION

Massive stars ( $>8 M_{\odot}$ ) play a crucial role in the evolution of their host galaxies, but their exact formation and evolution mechanisms are still under debate (Zinnecker & Yorke 2007; Peters et al. 2012; Dale 2015; Kuiper et al. 2015). It is not yet understood whether the formation of massive stars is only a scaled-up version of birth process of low mass stars, or is it a completely different process. One can find more details about the current theoretical scenarios of massive star formation in the recent reviews by Zinnecker & Yorke (2007) and Tan et al. (2014). Recently, a collision between two molecular clouds followed by a strong shock compression of gas is considered as a probable formation mechanism of massive stars (Furukawa et al. 2009; Ohama et al. 2010; Fukui et al. 2014; Torii et al. 2015). Habe & Ohta (1992) numerically found that the head-on collision between two non-identical molecular clouds can trigger the formation of massive stars, and such process could also form a broken bubble-like structure. In a detailed study of RCW 120 star-forming region using the molecular line data, Torii et al. (2015) reported that the

collision between two nearby molecular clouds has triggered the formation of an O star in RCW 120 in a short time scale. However, observational evidences for the formation of O stars via a collision between two molecular clouds are still very rare.

Massive stars can significantly influence the surrounding interstellar medium (ISM) through their energetics such as ionizing radiation, stellar winds, and radiation pressure. They have an ability to help in accumulation of surrounding materials (i.e., positive feedback) and/or to disperse matter into the ISM. Furthermore, they can also affect the star formation positively and negatively (Deharveng et al. 2010). The positive feedback of massive stars can trigger the birth of a new generation of stars including young massive star(s). More details about the various processes of triggered star formation can be found in the review article by Elmegreen (1998). However, the feedback processes of massive stars are not yet well understood, and the direct observational proof of triggered star formation by massive stars is rare. But the influence of massive stars on their surroundings can be studied with several other observational signatures (like H II region, wind-blown or radiation driven Galactic bubble, etc.).

Recently, *Spitzer* observations have revealed thousands of ring/shell/bubble-like structures in the 8  $\mu\text{m}$  images (Churchwell et al. 2006, 2007; Simpson et al. 2012), and many of them often enclose the H II regions. Hence, the bubbles associated with H II regions are potential targets to probe the physical processes governing the interaction and feedback effect of massive stars on their surroundings. Additionally, these sites are often grouped with the infrared dark clouds (IRDCs) and young stellar clusters, which also allow to understand the formation and evolution of these stellar clusters.

In this paper, we present a multi-wavelength study of such a mid-infrared (MIR) bubble, N37 ( $l = 25^\circ.292$ ,  $b = 0^\circ.293$ ; Churchwell et al. 2006), which is associated with an H II region, G025.292+00.293 (Churchwell et al. 2006; Deharveng et al. 2010; Beaumont & Williams 2010). The bubble N37 is classified as a broken or incomplete ring with an average radius and thickness of 1.77 and 0.49, respectively (Churchwell et al. 2006). The bubble is found in the direction of the H II region RCW 173 (Sh2-60) (see Figure 9 in Marco & Negueruela 2011). The velocity of the ionized gas ( $\sim 39.6 \text{ km s}^{-1}$ ; Hou & Han 2014) is in agreement with the line-of-sight velocity of the molecular gas ( $\sim 41 \text{ km s}^{-1}$ ; Beaumont & Williams 2010; Shirley et al. 2013) towards the bubble N37, indicating the physical association of the ionized and molecular emissions. Presence of several IRDCs are also reported around the N37 bubble by Peretto & Fuller (2009). Marco & Negueruela (2011) analyzed the photometry and spectroscopy of stars in the direction of the H II region, RCW 173, and found that most of the stars in the field are reddened B-type stars. They also identified a star a805 (G025.2465+00.3011) having spectral type of O7II and suggested this as the main ionizing source in the area. Several kinematic distances (2.6, 3.1, 3.3, 12.3, and 12.6 kpc) to the region are listed in the literature (e.g. Beaumont & Williams 2010; Churchwell et al. 2006; Blitz et al. 1982; Watson et al. 2010; Deharveng et al. 2010). However, it has been pointed out by Churchwell et al. (2006) that the MIR bubbles located at the Galactic plane are likely to be veiled behind the foreground diffused emission if they are situated at a distance larger than  $\sim 8$  kpc. Hence, it is unlikely for the bubble N37 to be located at a distance of about 12 kpc. Therefore, in this work, we have adopted a distance of 3.0 kpc, the average value of all available near-kinematic distance estimates.

We infer from the previous studies that the bubble is associated with an H II region and an IRDC together. However, the physical conditions inside and around the bubble N37 are not yet known, and the ionizing source(s) of the bubble is yet to be identified. Furthermore, the impact of the energetics of massive star(s) on its local environment is not yet explored. The detailed multi-wavelength study of the region will allow us to study the ongoing physical processes within and around the bubble N37. To study the physical environment and star formation mechanisms around the bubble, we employ multi-wavelength data covering from the optical, near-infrared (NIR) to radio wavelengths.

The paper is presented in the following way. In Section 2, we describe the details of the multi-wavelength data. We discuss the overall morphology of the region

in Section 3. In Section 4, we present the main results of our analysis. The possible star formation scenarios based on the multi-wavelength outcomes are discussed in Section 5. Finally, we conclude in Section 6.

## 2. OBSERVATIONS AND DATA REDUCTION

In this work, we employed a multi-wavelength data to have a detailed understanding of the ongoing physical processes within and around the bubble. We selected a large-scale region of  $15' \times 15'$  (centered at  $l = 25^\circ.315$ ,  $b = 0^\circ.278$ ) around the bubble N37, which also contains an IRDC and a pillar-like structure (see Figure 1a). Details of the new observations and the various archival data are described in the following sections.

### 2.1. Optical spectra

To spectroscopically identify the ionizing sources of the bubble N37, we obtained the optical spectra of two point-like sources ( $V \sim 14$  mag) using Grism 7 and Grism 8 of the Hanle Faint Object Spectrograph and Camera (HFOSC; with slit width of 167  $\mu\text{m}$  average spectral resolution is  $\sim 1000$ ) attached to the 2m Himalayan *Chandra* Telescope (HCT)<sup>1</sup>. Corresponding dark and flat frames were also obtained for dark-subtraction and flat-field corrections. The reduction of these spectra was performed using a semi-automated PyRAF based pipeline (Ninan et al. 2014).

### 2.2. Archival Data

We obtained the multi-wavelength data from the various Galactic plane surveys. In the following, we provide a brief description of these various archival data.

#### 2.2.1. Near-infrared Imaging Data

NIR photometric *JHK* magnitudes of point-like sources were collected from the United Kingdom Infrared Telescope (UKIRT) Infrared Deep Sky Survey (UKIDSS) Galactic Plane Survey (GPS release 6.0; Lawrence et al. 2007) catalog. The UKIDSS observations were carried out using the Wide Field Camera (WFCAM; Casali et al. 2007) attached to the 3.8m UKIRT telescope. Spatial resolution of the UKIDSS images is  $\sim 0''.8$ . Only good photometric magnitudes of point sources in the selected region were obtained following the conditions given in Lucas et al. (2008) and Dewangan et al. (2015). Several bright sources were saturated in the UKIDSS frames. Hence, the UKIDSS sources having magnitudes brighter than  $J = 13.25$ ,  $H = 12.75$  and  $K = 12.0$  mag were replaced by the Two Micron All Sky Survey (2MASS; Skrutskie et al. 2006) values.

#### 2.2.2. Near-infrared narrow band image

We retrieved the  $\text{H}_2$  (1–0) S(1) 2.122  $\mu\text{m}$  continuum-subtracted image from the UKIRT Wide-field Infrared Survey for  $\text{H}_2$  (UWISH2; Froebrich et al. 2011) archive. These observations were carried out using the WFCAM (Casali et al. 2007) on the UKIRT.

#### 2.2.3. Near-infrared Polarization Data

The *H*-band linear polarization data for point sources (resolution  $\sim 1''.5$ ) are also used in this study. The

<sup>1</sup> <https://www.iiap.res.in/iao-telescope>

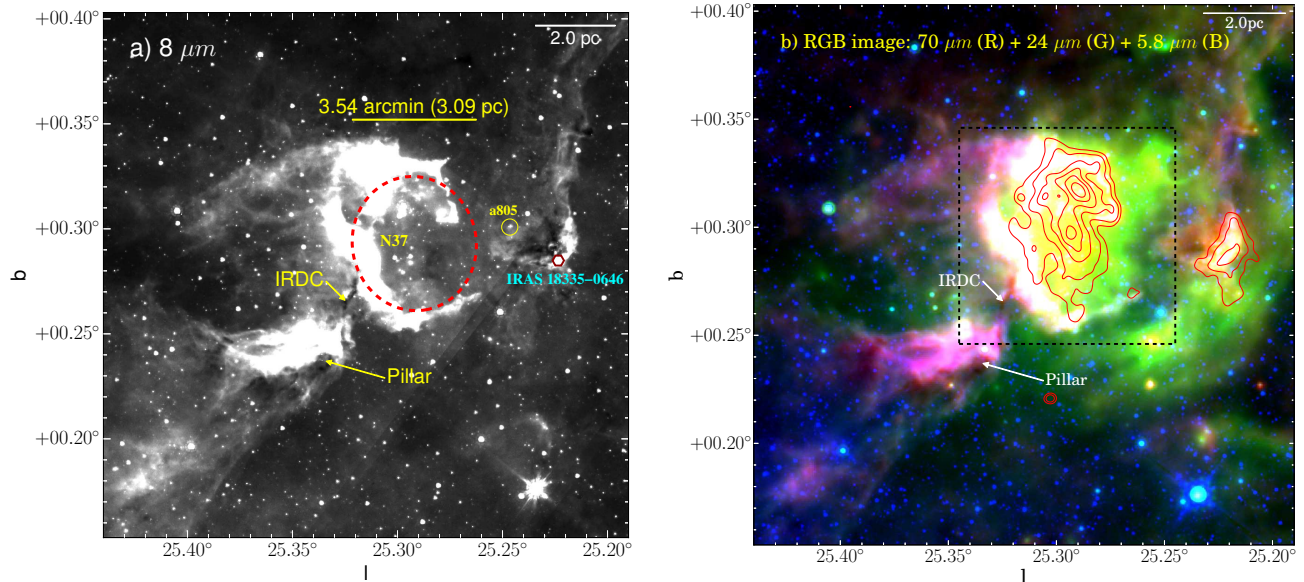


**Figure 1.** A MIR and FIR view of the region around the bubble N37 (selected area  $\sim 15' \times 15'$ ; centered at  $l = 25^\circ.315$ ,  $b = 0^\circ.278$ ). (a) The position of the bubble (from Churchwell et al. 2006) is highlighted by a red dashed ellipse in the *Spitzer*  $8 \mu\text{m}$  image. The star a805 (O7II spectral type; Marco & Negueruela 2011) is highlighted in the figure. Position of the IRAS 18335–0646 is also marked. (b) Three-color composite image (red: *Herschel*  $70 \mu\text{m}$ ; green: MIPS GAL  $24 \mu\text{m}$ ; blue: GLIMPSE  $5.8 \mu\text{m}$ ) of the region around the bubble. The MAGPIS 20 cm radio continuum emission is shown by red contours with levels of  $3.5\sigma$ ,  $4\sigma$ ,  $5\sigma$ ,  $6\sigma$ ,  $7\sigma$  and  $8\sigma$  (where,  $1\sigma=0.5 \text{ mJy/beam}$ ). The ionized emission is distributed inside the MIR bubble. The black dotted square represents the area of Figure 3. The pillar-like structure and IRDC are also marked in both the panels. A scale bar corresponds to 2 pc (at a distance of 3 kpc) is also shown in both the images.

polarization observations were performed using the 1.8m Perkins telescope operated by the Boston University and the corresponding data are available in the Galactic Plane Infrared Polarization Survey (GPIPS; Clemens et al. 2012) archive. In our analysis, we only considered sources having good polarization measurements with  $P/\sigma_P \geq 2.5$  (where  $P$  is the degree of polarization and  $\sigma_P$  is the corresponding uncertainty) and Usage Flag (UF) of 1.

#### 2.2.4. Mid-infrared Data

We retrieved the 3.6, 4.5, 5.8 and 8.0  $\mu\text{m}$  images and photometric magnitudes of point sources from the *Spitzer*-Galactic Legacy Infrared Mid-Plane Survey Extraordinaire (GLIMPSE; Benjamin et al. 2003) survey (spatial resolution  $\sim 2''$ ). The photometric magnitudes were obtained from the GLIMPSE-I Spring '07 highly reliable catalog. In addition to the GLIMPSE data, the Multiband Infrared Photometer for *Spitzer* (MIPS) Inner Galactic Plane Survey (MIPSGAL; Carey et al. 2005) images at  $24 \mu\text{m}$  (resolution  $\sim 6''$ ) and the magnitudes of point sources at  $24 \mu\text{m}$  (Gutermuth & Heyer 2015) are also used in the analysis. Some sources, which are well detected in the  $24 \mu\text{m}$  image, do not have photometric magnitudes in the MIPSGAL  $24 \mu\text{m}$  catalog of Gutermuth & Heyer (2015). Hence, we separately performed the photometric reduction of  $24 \mu\text{m}$  image of the N37 region. A detailed procedure of this photometric reduction can be found in Dewangan et al. (2012).

#### 2.2.5. Far-infrared and millimeter data

In order to construct the dust temperature and column density maps of the N37 region, we utilized level2.5 processed *Herschel* 70–500  $\mu\text{m}$  images. The beam sizes of images at 70, 160, 250, 350, and 500  $\mu\text{m}$  are  $5''.8$ ,  $12''$ ,  $18''$ ,  $25''$ , and  $37''$  (Poglitsch et al. 2010; Griffin et al. 2010), respectively.

We have also obtained the APEX Telescope Large Area Survey of Galaxy (ATLASGAL; Schuller et al. 2009) 870  $\mu\text{m}$  continuum image (beam  $\sim 19''.2$ ) and the Bolocam 1.1 mm (Aguirre et al. 2011) image (beam  $\sim 33''$ ) of the region around the bubble.

#### 2.2.6. Molecular line data

The  $^{13}\text{CO}$  ( $J=1-0$ ) line data were retrieved from the Galactic Ring Survey (GRS; Jackson et al. 2006). The GRS data have a velocity resolution of  $0.21 \text{ km s}^{-1}$ , an angular resolution of  $45''$  with  $22''$  sampling, a main beam efficiency ( $\eta_{\text{mb}}$ ) of  $\sim 0.48$ , a velocity coverage of  $-5$  to  $135 \text{ km s}^{-1}$ , and a typical rms sensitivity ( $1\sigma$ ) of  $\approx 0.13 \text{ K}$ .

#### 2.2.7. Radio continuum data

The Very Large Array (VLA) 20 cm radio continuum map (beam size  $\sim 6''.2 \times 5''.4$ ) of the N37 region was obtained from the Multi-Array Galactic Plane Imaging Survey archive (MAGPIS; Helfand et al. 2006).

### 3. MORPHOLOGY OF THE REGION

A detailed understanding of the ongoing physical processes in a given star-forming region requires a thorough and careful multi-wavelength investigation of the region. In a star-forming region, the spatial distribution of the ionized, dust, and molecular emission allows us to identify the H II regions and cold embedded condensations, which further help us to infer the physical conditions of the region. A multi-wavelength picture of the region around the bubble is presented in Figures 1 and 2. In Figure 1a, on a larger scale, the  $8.0 \mu\text{m}$  image shows a pillar-like structure, an IRDC, an IRAS source (IRAS 18335–0646), and the MIR bubble N37. The broken or incomplete ring morphology of N37 bubble is clearly seen in the image, as previously reported by Churchwell et al.

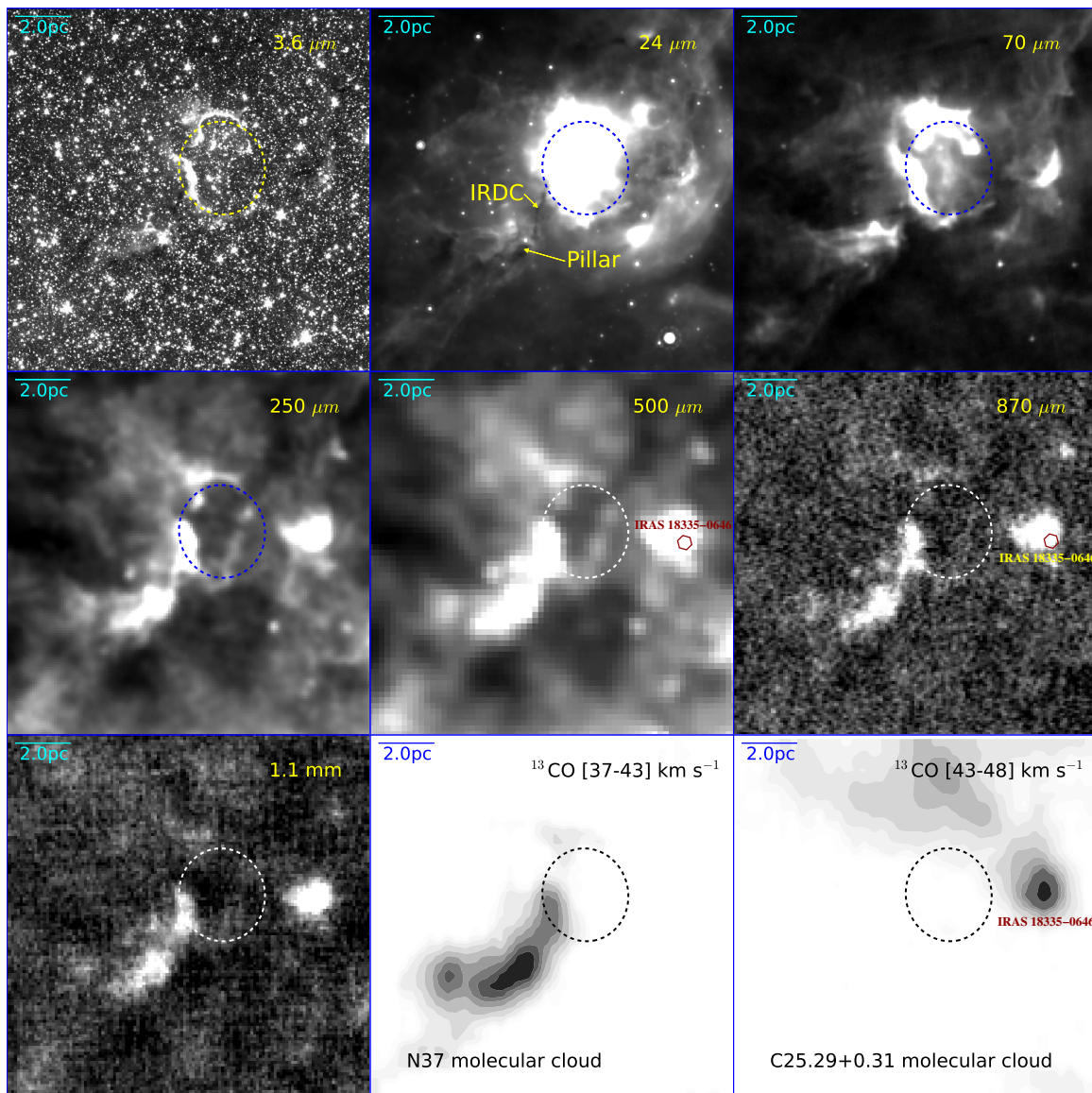


**Figure 2.** Distribution of the warm and cold dust emission towards the N37 region. The images were obtained from the *Spitzer* (3.6–24  $\mu\text{m}$ ), *Herschel* (70–500  $\mu\text{m}$ ), ATLASGAL (870  $\mu\text{m}$ ), and BOLOCAM (1.1 mm) survey archives. Last two bottom panels show solid contour maps of the integrated  $^{13}\text{CO}$  emission in the velocity ranges of 37–43 and 43–48  $\text{km s}^{-1}$ , respectively. The remaining symbols are similar to those shown in Figure 1.

(2006). Figure 1b shows the spatial distribution of the warm dust towards the N37 region (RGB map: 70  $\mu\text{m}$  in red; 24  $\mu\text{m}$  in green; 5.8  $\mu\text{m}$  in blue). The MAGPIS 20 cm radio continuum emission is also overlaid on the RGB map, which depicts the distribution of the ionized emission. The periphery of the bubble is dominated by the 5.8  $\mu\text{m}$  emission and encloses the warm dust as well as the ionized gas. In general, the polycyclic aromatic hydrocarbon (PAH) features are seen at 3.3, 6.2, 7.7, and 8.6  $\mu\text{m}$  and trace a photodissociation region (PDR) surrounding the ionized gas. Hence, the emission seen in the 5.8 and 8.0  $\mu\text{m}$  images might be tracing a PDR towards the N37 bubble.

A longer wavelength view (250–1100  $\mu\text{m}$ ) of the region is presented in Figure 2. The images at 3.6–70  $\mu\text{m}$  are also shown for comparison with the submillimeter and millimeter wavelength images. The emission at 250–1100  $\mu\text{m}$  traces cold dust components (see Section 4.5

for quantitative estimates). The cold dust emission is mainly seen towards the pillar-like structure and the IRAS 18335–0646. Note that the ionized emission is also detected towards the IRAS 18335–0646 (see Figure 1b). We utilized the GRS  $^{13}\text{CO}$  ( $J=1-0$ ) line data to infer the physical association of different subregions seen in our selected region around the bubble N37. Based on the velocity information of  $^{13}\text{CO}$  data, we find that there are two molecular clouds present in our selected region. The molecular cloud associated with the bubble (i.e. N37 molecular cloud) is traced in the velocity range of 37–43  $\text{km s}^{-1}$ . However, the molecular cloud associated with the IRAS 18335–0646 (also referred as C25.29+0.31 in Anderson et al. 2009) is traced in the velocity range from 43 to 48  $\text{km s}^{-1}$ . In the last two bottom panels, we show the velocity integrated  $^{13}\text{CO}$  maps of the two clouds seen in our selected region around the bubble. The integrated  $^{13}\text{CO}$  emission map reveals an elongated morphology of

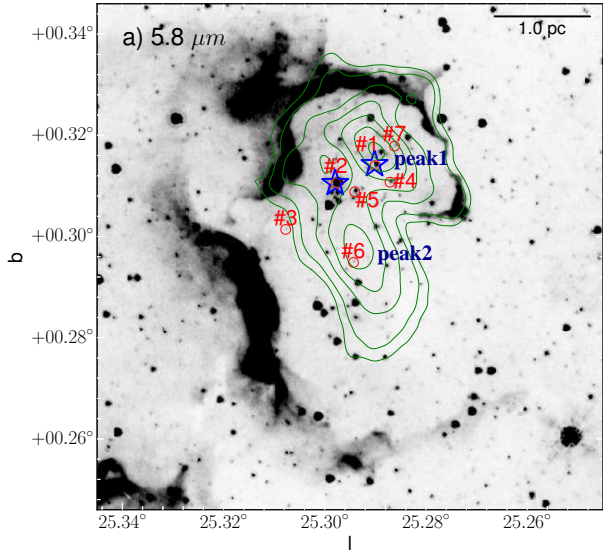


**Figure 3.** Photometrically identified OB stars are marked by open circles and are labeled by numbers (as per their respective serial numbers in Table 1) on the *Spitzer*-IRAC  $5.8 \mu\text{m}$  image. The MAGPIS 20 cm radio contours are also overlaid on the image. Asterisks represent the sources for which optical spectroscopic observations were performed (see Figure 4).

the N37 molecular cloud (i.e. velocity range  $\sim 37\text{--}43 \text{ km s}^{-1}$ ), which hosts the pillar-like structure, an IRDC, and the bubble N37.

On the other hand, the integrated  $^{13}\text{CO}$  map of the C25.29+0.31 cloud traces a large condensation associated with the IRAS 18335–0646, as seen in the longer wavelength continuum images (see Figure 2). Wienen et al. (2012) also reported the  $\text{NH}_3$  line parameters such as  $\text{NH}_3(1,1)$  radial velocity  $\sim 46.13 \text{ km s}^{-1}$  and kinematic temperature ( $T_{\text{kin}}$ )  $\sim 21.76 \text{ K}$  toward the ATLASGAL condensation associated with the IRAS 18335–0646. These results suggest that the condensation associated with the IRAS 18335–0646 is not physically linked with the bubble N37.

A more detailed analysis of these two molecular clouds (i.e. N37 molecular cloud and C25.29+0.31) is discussed in the Section 4.8.

#### 4. RESULTS

In this section, we present the outcomes of our multi-wavelength analysis in the following way. First, we present the results related to the identification of ionizing source(s) of the region, and then the origin of the N37 bubble. Next, we present the column density and the temperature maps of the region to identify the cold condensations. We have also identified young stellar objects (YSOs) towards the region, and construct the surface density map of these YSOs to study their spatial distribution. Finally, we examine the NIR polarization data and the  $^{13}\text{CO}$  molecular line data to examine the large scale magnetic field morphology and the kinematics of CO gas, respectively.

##### 4.1. Identification of ionizing candidates

We have seen that the ionized emission is enclosed within the N37 bubble (see Figure 1b) and two prominent peaks (i.e. peak1 and peak2 shown in Figure 3) are seen in the radio continuum map. To search for pos-

sible OB type candidates located within the N37 bubble, we performed a photometric method to identify the probable ionizing candidates of the region, following a similar procedure outlined in Dewangan & Ojha (2013). The analysis was carried out using the NIR and MIR photometric magnitudes of point sources from the UKIDSS and GLIMPSE catalogs, respectively. We only considered the sources located near the radio emission peaks and detected at least in five photometric bands among UKIDSS JHK and *Spitzer*-IRAC 3.6, 4.5 and  $5.8 \mu\text{m}$  bands. Following this condition, a total of seven sources were identified, and these are marked and labeled in Figure 3. The extinction to these sources were estimated assuming intrinsic colors of  $(J-H)_0$  and  $(H-K)_0$  for O- and B-stars from Martins & Plez (2006) and Pecaut & Mamajek (2013), respectively, and using the extinction law ( $A_J/A_V = 0.284$ ,  $A_H/A_V = 0.174$ ,  $A_K/A_V = 0.114$ ) from Indebetouw et al. (2005). The absolute JHK magnitudes of all these sources were calculated assuming a distance of 3.0 kpc and were compared with those listed in Martins & Plez (2006, for O stars), and Pecaut & Mamajek (2013, for B stars). We found that two O-type and five B-type stars are located near the radio peaks within the N37 bubble. All these sources with their photometric magnitudes and derived spectral types are listed in Table 1. Note that a single distance is assumed for all the sources, and the spectral types are also estimated without considering the photometric uncertainties of intrinsic colors and observed magnitudes of these sources. Spectroscopic observations will be helpful to further confirm the spectral type of these sources (see Section 4.2).

##### 4.2. Spectroscopy of ionizing candidates

We have carried out optical spectroscopic observations (4000–7500 Å) of two brightest photometrically identified OB stars (see asterisks in Figure 3). The remaining five sources are beyond the limit of optical spectroscopic capability of the HCT (V-limit  $\simeq 18\text{-mag}$  for spectrum having signal-to-noise ratio of about 20 with 30 min exposure). The observed spectra of these two sources are shown in Figure 4. One of these sources (source #1) is situated near the peak1 ( $\sim 10''$ ) of the 20 cm radio emission, and the other one (#2) is located  $\sim 36''$  away from the radio peak1.

Several hydrogen and helium lines are found in both the spectra (Figures 4a and 4b). The presence of hydrogen lines is generally seen in early type sources (O–A spectral type), however, the existence of He I-II lines is not found in A stars (Walborn & Fitzpatrick 1990). Note that the ionization of helium requires a high temperature generally seen in O-type sources. To confirm the spectral types of these sources, we further compared our observed spectra with the available OB stars’ spectra (Walborn & Fitzpatrick 1990; Pickles 1998). Generally, spectral lines in the first part of the optical spectrum (4000–5500 Å) are used to determine the spectral type of any source. However, the signal-to-noise ratio of the first part of both the spectra is not very good, possibly because of large visual extinction toward the region. A visual comparison of the observed spectra with the available library spectra reveals that the source #1 is likely to be a O9V star, while the other source (#2) is an B0V

**Table 1**  
Details of the photometrically identified OB stars toward the N37 region.

Sr. No.	RA (J2000) (hh:mm:ss)	Dec (J2000) (dd:mm:ss)	J (mag)	H (mag)	K (mag)	[3.6] (mag)	[4.5] (mag)	[5.8] (mag)	[8.0] (mag)	$A_V$ (mag)	$M_J$ (mag)	$M_H$ (mag)	$M_K$ (mag)	Sp. Type
1	18:36:18.6	-06:39:09	10.17	9.62	9.34	10.17	9.62	9.34	9.24	6.11	-3.95	-3.84	-3.74	O8V <sup>a</sup>
2	18:36:20.2	-06:38:50	10.41	9.80	9.38	10.41	9.80	9.38	8.15	7.49	-4.10	-3.90	-3.86	O7V-O8V <sup>b</sup>
3	18:36:23.3	-06:38:34	15.23	13.44	12.55	15.51	13.53	12.70	11.91	16.20	-1.76	-1.80	-1.67	B2V
4	18:36:19.0	-06:39:24	13.61	12.64	11.92	13.76	12.62	11.93	11.06	11.05	-1.92	-1.70	-1.73	B2V
5	18:36:20.2	-06:39:05	14.12	12.88	12.14	13.73	12.42	11.73	–	12.45	-1.80	-1.70	-1.66	B2V
6	18:36:23.2	-06:39:27	14.52	12.98	12.20	14.42	12.71	11.94	11.38	14.21	-1.90	-1.90	-1.81	B2V
7	18:36:17.4	-06:39:15	15.29	13.18	12.08	15.20	13.04	11.94	11.18	19.77	-2.71	-2.69	-2.56	B1V

<sup>a</sup> Spectroscopically identified O9V

<sup>b</sup> Spectroscopically identified B0V

candidate. It can be seen in Section 4.1 that the second source was photometrically identified as O7-8V star possibly because of the assumed distance of 3.0 kpc in the calculation which might not be true (see next paragraph).

We have also estimated spectro-photometric distances to these two sources. The optical BV-band magnitudes of both the sources were obtained from the American Association of Variable Stars Observers (AAVSO) Photometric All-Sky Survey (APASS) catalog (DR9) and the NIR  $K$ -band magnitudes were collected from the 2MASS catalog. To estimate the distance to the O9V source, we first obtained the intrinsic color of an O9V star ( $(V - K)_o \sim -0.79$ ) from Wegner (1994). Furthermore, the color excess  $E(B - V)$  was estimated using the relation  $E(V - K)/E(B - V) \sim 2.826$  given in Wegner (1994). Though it is debatable whether the value of  $R_V$  ( $A_V/E(B - V)$ ) is 3.1 all over the Galaxy or is it substantially different in Galactic star-forming regions (see Pandey et al. 2003, and references therein), we considered the mean  $R_V$  of 3.1 itself for the reddening correction. Accordingly, the visual extinction of the source was found to be 6.3 mag. The absolute and apparent V-band magnitudes of both the sources were obtained from Lang (1999) and the APASS catalog, respectively. With an absolute V-magnitude of -4.5 and apparent V-magnitude of 14.37, we estimated the distance to the O9V star of 3.1 kpc. Following the similar procedure for the other source (B0V) with the absolute and apparent magnitudes of -4.0 and 14.55, respectively, the visual extinction ( $A_V$ ) was estimated to be 6.4 mag, and the corresponding distance to the source is 2.7 kpc. Note that large errors (at least 20%) could be associated with these distance estimates due to photometric uncertainties, and the general extinction law used in the estimation. However, similar distances of these sources and the bubble suggest that they are physically associated with the N37 bubble.

#### 4.3. Radio continuum emission and the dynamical age

The integrated radio continuum flux is used as a tool to determine the spectral type of the source responsible to develop the H II region. The presence of an H II region is traced in the MAGPIS 20 cm map (see Figure 1b). The Lyman continuum flux (photons  $s^{-1}$ ) required for the observed radio continuum emission is estimated following

the equation given in Moran (1983):

$$S_{Lyc} = 8 \times 10^{43} \left( \frac{S_\nu}{mJy} \right) \left( \frac{T_e}{10^4 K} \right)^{-0.45} \left( \frac{D}{kpc} \right)^2 \left( \frac{\nu}{GHz} \right)^{0.1} \quad (1)$$

where  $\nu$  is the frequency of observations,  $S_\nu$  is the total observed flux density,  $T_e$  is the electron temperature, and  $D$  is the distance to the source. Here, the region is assumed to be homogeneous and spherically symmetric, and a single main-sequence star is responsible for the observed free-free emission. The flux density ( $S_\nu$ ) and the size of the H II region are determined using the JMFIT task of the Astronomical Image Processing Software (AIPS). Typical value of the electron temperature,  $T_e \sim 10000$  K for a classical H II region (Stahler & Palla 2005) is adopted in the calculation. The spectral type of the powering source is finally estimated by comparing the observed Lyman continuum flux with the theoretical value for solar abundance given in Smith et al. (2002).

In the MAGPIS 20 cm map, two radio peaks are clearly evident within the bubble (peak1 and peak2; see Figure 3), and we estimated the spectral type of the possible ionizing source for both the peaks separately. The Lyman continuum flux for the radio peak1 ( $S_\nu \sim 1.18$  Jy;  $S_{Lyc} \sim 10^{47.95}$  photons  $sec^{-1}$ ) corresponds to an ionizing source having spectral type of O9V, while the ionizing source corresponding to the radio peak2 ( $S_\nu \sim 0.56$  Jy;  $S_{Lyc} \sim 10^{47.62}$  photons  $sec^{-1}$ ) is a B0V star.

As mentioned before (see Sections 4.1 and 4.2), using the spectroscopy and photometry, we identified three OB stars (O9V, B1V, and B2V) that are located near the radio peak1 (see Figure 3). However, the Lyman continuum flux (Smith et al. 2002) expected together from solar abundant B1V and B2V stars is about an order less compared to the O9V star, and therefore, the total flux is mainly dominated by the O9V star. Hence, it seems that an O9V star located at a distance of  $\sim 10''$  from the radio peak1 is the primary ionizing source of the region. The spectral type of the ionizing source determined from the radio analysis is consistent with our spectroscopic results. Toward the radio peak2, we identified a B2V star using the photometric analysis, however the estimation from the radio continuum flux shows the ionizing source to be a B0V star. The spectral type corresponding to the peak2 estimated using two methods is showing inconsistency because the photometric determinations of spectral types may vary substantially depending on the distance to the source and the photometric accuracy.

We have also determined the dynamical age of the H II

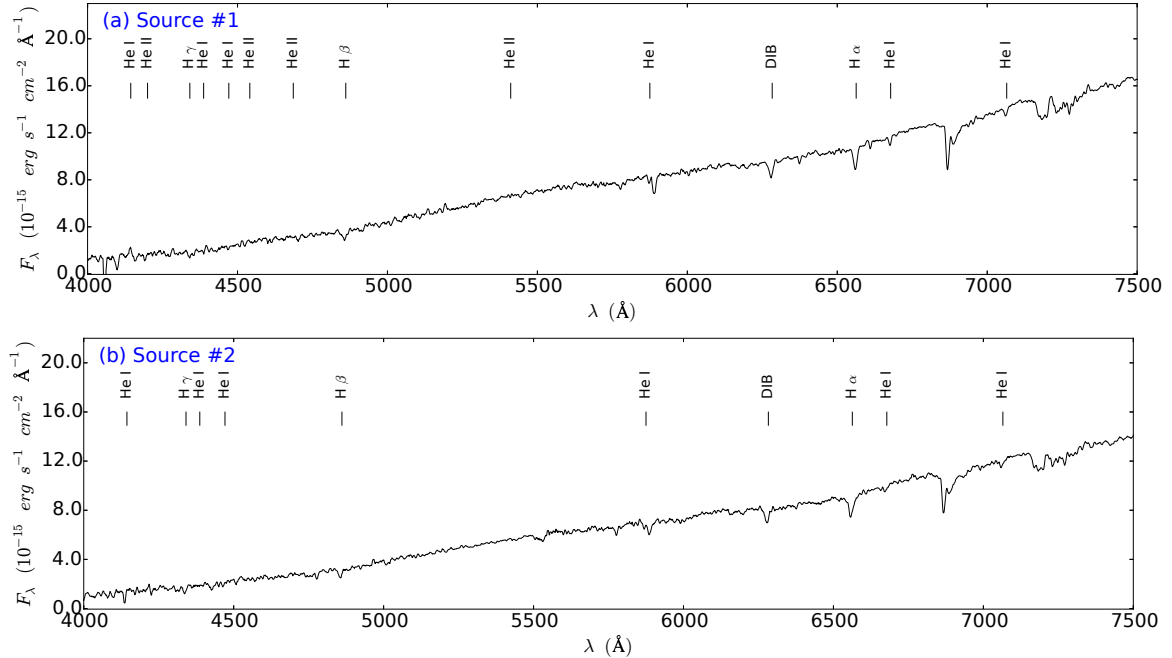


**Figure 4.** Optical spectra of sources #1 (a) and #2 (b) (as marked in Figure 3) observed using the HFOSC mounted on the 2-m HCT. Several prominent hydrogen and helium lines are detected in both the spectra.

region using the MAGPIS 20 cm data. A massive source ionizes the surrounding gas, and develop an H II region. The ionization front of the H II region expands until an equilibrium is achieved between the rate of ionization and recombination. Theoretical radius of the H II region (i.e., Strömgen radius; Strömgen 1939) for a uniform density and temperature, can be written as:

$$R_S = \left( \frac{3S_{Lyc}}{4\pi n_0^2 \beta_2} \right)^{1/3} \quad (2)$$

where  $n_0$  is the initial ambient density, and  $\beta_2$  is the recombination coefficient. For a temperature of 10,000 K, the value of  $\beta_2$  is  $2.60 \times 10^{-13} \text{ cm}^3 \text{ s}^{-1}$  (Stahler & Palla 2005).

A shock front is generated because of the large temperature and pressure gradient between the ionized gas and the surrounding cold material, and the shock front is further propagated into the surroundings. The corresponding radius of the ionized region at any given time can be written as (Spitzer 1978):

$$R(t) = R_S \left( 1 + \frac{7c_{II}t_{dyn}}{4R_S} \right)^{4/7} \quad (3)$$

where the speed of sound in an H II region ( $c_{II}$ ) is  $11 \times 10^5 \text{ cm s}^{-1}$  (Stahler & Palla 2005) and  $t_{dyn}$  is the dynamical age of the H II region. The size of the H II region, i.e.,  $R(t)$ , was estimated to be 1.4 pc by using the JMFIT task of the AIPS. Note that the calculated dynamical age can vary substantially depending on the initial value of the ambient density. Therefore, we estimated the Strömgen radius and the corresponding dynamical age for a range of ambient density starting from 1000 to 10000  $\text{cm}^{-3}$  (e.g. classical to ultra-compact H II regions; Kurtz 2002). For the corresponding densities, the dynamical age varies from 0.21–0.71 Myr. However, the Strömgen radius and dynamical age were calculated by assuming the region as

homogeneous and spherically symmetric. Hence, the dynamical age of the H II region should be considered as a representative value (see Section 5 for more discussion).

#### 4.4. Origin of the bubble

In Figure 5a, we present the continuum-subtracted  $\text{H}_2$  emission ( $2.122 \mu\text{m}$ ) map toward the bubble N37, which traces the edges of the bubble. The  $\text{H}_2$  features have similar morphology as seen in the *Spitzer*-GLIMPSE images. The  $\text{H}_2$  emission in a given star-forming region is originated in the shocked region developed at the interface of the ionized and cold matter. From the distribution of  $\text{H}_2$  emission,  $8.0 \mu\text{m}$  emission and the ionized emission (see Figure 2), it is evident that the emission seen in the narrow  $\text{H}_2$ -band is tracing the PDR towards the N37 region. Possibly, the  $\text{H}_2$  emission is originated in the shocked region developed due to the expansion of the ionized gas.

Ratio maps of *Spitzer*-IRAC images have ability to provide the information about the interaction of massive star(s) with its surrounding environment (Povich et al. 2007; Dewangan et al. 2012; Dewangan & Ojha 2013). Note that the *Spitzer*-IRAC bands contain several prominent characteristic atomic and molecular lines. For example, IRAC Ch1 contains a PAH feature at  $3.3 \mu\text{m}$  as well as a prominent molecular hydrogen line at  $3.234 \mu\text{m}$  ( $\nu = 1-0 O(5)$ ). IRAC Ch2 also contains a molecular hydrogen emission line at  $4.693 \mu\text{m}$  ( $\nu = 0-0 S(9)$ ) generally excited by outflow shocks, and a hydrogen recombination line  $\text{Br}\alpha$  ( $4.05 \mu\text{m}$ ). Figure 5b shows the IRAC Ch2/Ch1 ratio map of the N37 region, which reveals the bright emission region surrounded by the dark features. In general, the dark regions in the  $4.5 \mu\text{m}/3.6 \mu\text{m}$  ratio map traces the excess  $3.6 \mu\text{m}$  emission, while the bright emission region suggests the domination of  $4.5 \mu\text{m}$  emission. The bright emission region in the ratio map is very well correlated with the radio continuum emission. Therefore, it seems that this bright emission

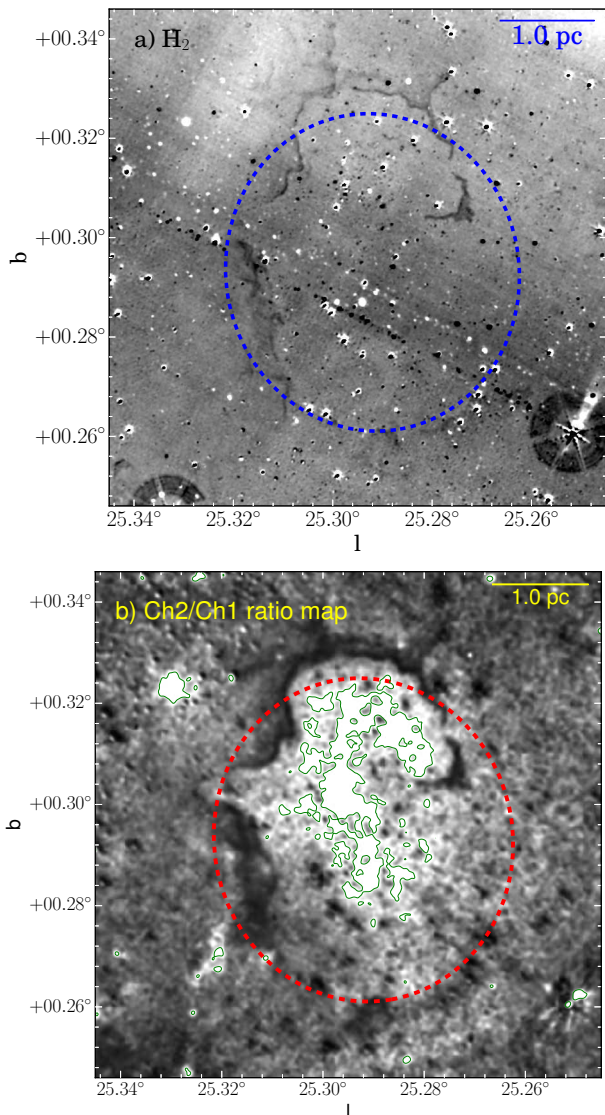


**Figure 5.** (a) Inverted continuum-subtracted H<sub>2</sub>-band ( $\nu = 1-0 S(1)$ ) at  $2.122 \mu\text{m}$  image of the N37 region. (b) *Spitzer*-IRAC Ch2/Ch1 ratio map of the N37 region. In the ratio map, the bright emission region is traced by contours. The interior of the bubble is traced with ratio greater than 1.1, while the periphery of the bubble is traced with ratio less than 0.8.

region probably traces the Br $\alpha$  feature originated by the photoionized gas. The dark features in the ratio map are also well correlated with the  $2.122 \mu\text{m}$  H<sub>2</sub> emission, indicating that the ratio map probably traces the H<sub>2</sub> features (see Figures 5a and 5b). However, it must be noted that the Ch1 also contains  $3.3 \mu\text{m}$  PAH emission feature which may also contribute to the dark features seen in the ratio map. Overall, we found that the IRAC ratio map and the continuum-subtracted H<sub>2</sub> image trace PDR around the H II region.

Massive stars can influence their parent molecular clouds via different feedback components - (i) pressure due to radiation ( $P_{rad}$ ), (ii) pressure due to HII region ( $P_{HII}$ ), and (iii) pressure due to wind ( $P_{wind}$ ). It is important to determine the strongest pressure component of massive stars in order to have a better knowledge of the feedback mechanisms. Pressure due to radiation can be formulated as  $P_{rad} = L_{bol}/4\pi cD_s^2$ , where  $L_{bol}$  is the

bolometric luminosity and  $D_s$  is the distance from the star to the region of interest. Similarly, the pressures due to the H II region and stellar wind can be written as  $P_{HII} = \mu m_H C_{II}^2 (3N_{UV}/4\pi\beta_2 D_s^3)^{1/2}$  and  $P_{wind} = \dot{M}_w V_w / 4\pi D_s^2$ , respectively, where the mean molecular weight in an H II region,  $\mu=0.678$  (Bisbas et al. 2009),  $C_{II}$  is the sound speed in an H II region =  $11 \text{ km s}^{-1}$ ,  $\beta_2$  is a recombination coefficient =  $2.6 \times 10^{-13} \text{ cm}^3 \text{ s}^{-1}$ ,  $N_{UV}$  is the number of UV photons,  $\dot{M}_w$  is the mass-loss rate of the source,  $V_w$  is the terminal velocity of the stellar wind (see Bressert et al. 2012, for more details about these formulas). All the pressure components were estimated at a distance of  $\sim 1 \text{ pc}$  which is the nearest edge of the bubble from the massive O9V star.

The pressure exhibited by the H II region with  $N_{UV} \sim 10^{48.12}$  photons  $\text{sec}^{-1}$  (i.e., total Lyman continuum for both the radio continuum peaks; see Section 4.3) is estimated to be  $2.8 \times 10^{-10} \text{ dyne cm}^{-2}$ . For the estimation of  $P_{rad}$ , the bolometric luminosities of all seven OB stars within the bubble were obtained from Lang (1999) and the total radiation pressure exhibited by all these OB stars is found to be  $1.8 \times 10^{-10} \text{ dyne cm}^{-2}$ . To estimate the combined  $P_{wind}$  from all the seven OB stars, the wind speed and the mass-loss rate for the O9V star were obtained from Muijres et al. (2012) ( $V_w \sim 1000 \text{ km s}^{-1}$ ;  $\dot{M}_w \sim 10^{-7.8} M_\odot \text{ yr}^{-1}$ ). The corresponding values for B0V, B1V and B2V stars ( $V_w \sim 1000, 700$  and  $700 \text{ km s}^{-1}$ ;  $\dot{M}_w \sim 10^{-9.3}, 10^{-9.4}, 10^{-9.7} M_\odot \text{ yr}^{-1}$ , respectively) were obtained from Oskinova et al. (2011). The combined pressure due to the wind ( $P_{wind}$ ) from all the seven OB stars comes out to be  $5.1 \times 10^{-12} \text{ dyne cm}^{-2}$ . The estimation of different pressure components infers that the pressure due to the ionized gas (i.e., H II region) is the predominant component. However, there is also a substantial radiation pressure contributed together by all the OB stars. Note five out of seven of these OB stars not only lack of spectroscopic confirmations, but also association of them with the N37 bubble is uncertain. Therefore, the calculated values of the pressure due to the radiation and the stellar wind should be treated as upper limits. From the overall analysis it seems that a shock-front has been developed due to the expansion of the H II region which excites the H<sub>2</sub> emission as well as PAH emission. Our results indicate that the N37 bubble is possibly originated due to the ionizing feedback of the massive stars.

#### 4.5. Column density and temperature maps

We have constructed the column density and the temperature maps of the region using *Herschel* images to probe the condensations and the distribution of cold matter. A pixel-by-pixel modified blackbody fit was performed to the cold dust emission seen in the *Herschel* 160, 250, 350 and  $500 \mu\text{m}$  images. The  $70 \mu\text{m}$  image was not considered in our analysis because a substantial part of the  $70 \mu\text{m}$  flux comes from the warm dust. Before performing the fit, all the images were convolved to the lowest resolution of  $37''$  (beam size of the  $500 \mu\text{m}$  image) and converted to the same flux unit ( $\text{Jy pixel}^{-1}$ ). For better estimation of the source flux, we subtracted the corresponding background flux from each image (see Mallick et al. 2015, for more detail). Background flux

was estimated in a relatively dark region ( $l = 24^\circ.60$ ,  $b = 1^\circ.00$ ; area:  $10' \times 10'$ ) away from our selected target, and corresponding fluxes are  $-2.202$ ,  $1.328$ ,  $0.693$  and  $0.252$  Jy pixel $^{-1}$  for 160, 250, 350 and 500  $\mu\text{m}$  images, respectively.

Finally, the pixel-by-pixel basis modified black-body fitting was performed by using the formula (Battersby et al. 2011; Sadavoy et al. 2012; Nielbock et al. 2012; Launhardt et al. 2013):

$$S_\nu(\nu) - I_{bg}(\nu) = B_\nu(\nu, T_d)\Omega(1 - e^{-\tau(\nu)}) \quad (4)$$

where optical depth can be written as:

$$\tau(\nu) = \mu_{H_2} m_H \kappa_\nu N(H_2) \quad (5)$$

Different symbols in the above equations are as follows -  $S_\nu(\nu)$ : observed flux density,  $I_{bg}$ : background flux density,  $B_\nu(\nu, T_d)$ : Planck's function,  $T_d$ : dust temperature,  $\Omega$ : solid angle subtended by a pixel,  $\mu_{H_2}$ : mean molecular weight,  $m_H$ : mass of hydrogen,  $\kappa_\nu$ : dust absorption coefficient, and  $N(H_2)$ : column density. Here, we used  $\Omega = 4.612 \times 10^{-9}$  steradian (i.e. for  $14'' \times 14''$  area),  $\mu_{H_2} = 2.8$  and  $\kappa_\nu = 0.1 (\nu/1000 \text{ GHz})^\beta \text{ cm}^2 \text{ g}^{-1}$ , the gas-to-dust ratio of 100, and the dust spectral index  $\beta = 2$  for sources with thermal emission in the optically thick medium (Hildebrand 1983).

The final column density and temperature maps of the  $15' \times 15'$  area of the N37 region are shown in Figures 6a and 6b, respectively. Several condensations are seen towards the region. The 'clumpfind' software (Williams et al. 1994) has been used to identify the clumps and to measure the total column density in each clump. The mass of a clump is estimated using the formula (Mallick et al. 2015):

$$M_{clump} = \mu_{H_2} m_H Area_{pix} \Sigma N(H_2) \quad (6)$$

where  $\mu_{H_2} = 2.8$ ,  $Area_{pix}$  is the area subtended by one pixel, and  $\Sigma N(H_2)$  is the total column density of the clump obtained using the 'clumpfind'. A total of 17 clumps are identified toward the  $15' \times 15'$  area of the N37 region (see Figure 6). However, based on the integrated CO maps (see Figure 2), we find only five clumps (i.e. C2-5 and C10, in Figure 6) associated with the N37 molecular cloud, and the remaining clumps appear to be associated with the C25.29+0.31 molecular cloud. In the present work, our analysis is focused on the N37 molecular cloud, and hence, we do not discuss the results of the C25.29+0.31 cloud. In the N37 molecular cloud, the five associated clumps (i.e. C2-5 and C10;  $M_{clump}$  from  $\sim 1350$ - $2150 M_\odot$ ) are having temperatures and densities in the range from  $\sim 22$ - $23$  K and  $\sim 7.2$ - $9.5 \times 10^{21} \text{ cm}^{-2}$  (corresponding  $A_V \sim 8.0$ - $10.0$  mag), respectively. Here, to estimate the visual extinction, we use the relation  $\langle N(H_2)/A_V \rangle = 0.94 \times 10^{21} \text{ molecules cm}^{-2} \text{ mag}^{-1}$  (Bohlin et al. 1978).

#### 4.6. Young stellar population

The study of YSOs in a given star-forming region allows to characterize the area of the ongoing star formation. Hence, we have carried out identification of YSOs using the NIR and MIR color-magnitude and color-color schemes. A more elaborative description of these schemes is given below.

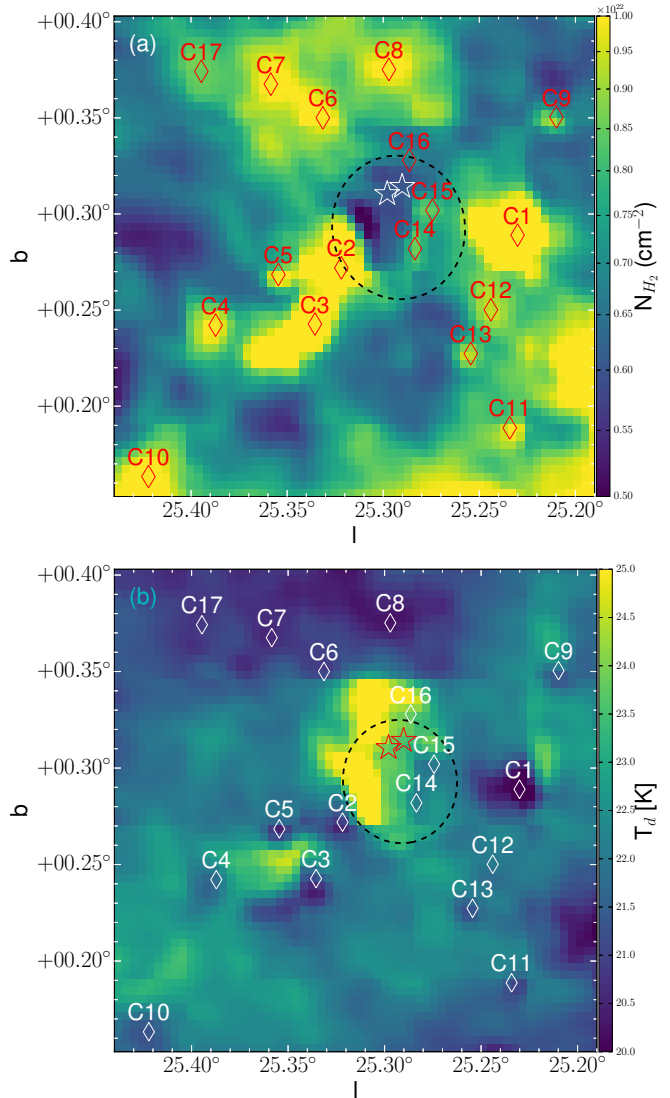


**Figure 6.** *Herschel* (a) column density and (b) temperature maps of the selected area around the N37 bubble. Several identified cold condensations are also marked ( $\diamond$ ) in both the maps.

#### 4.6.1. Selection of YSOs

Four different schemes are employed to identify and classify the YSOs for the selected  $15' \times 15'$  area around the N37 region.

1. Young sources are known to be a strong emitter at MIR bands, while they are still embedded in their parent molecular clouds and cannot be seen in the optical/NIR bands. Hence, MIR photometric criteria allow us to identify sources at a very early phase. We cross-matched the sources that have detections in both the MIPS GAL 24  $\mu\text{m}$  and *Spitzer*-IRAC/GLIMPSE 3.6  $\mu\text{m}$  bands, and constructed a color-magnitude diagram ( $[3.6] - [24]/[3.6]$ ) to identify the YSOs, following the color criteria given in Guieu et al. (2010) and Rebull et al. (2011). A total of 100 sources are found that are common in the 3.6 and 24  $\mu\text{m}$  bands. The color-magnitude diagram of these sources is shown in Figure 7a. Different classes of YSOs are marked by distinct symbols and are separated by black dashed-lines. The boundaries for other contaminants like disk-less stars and galaxies are also marked

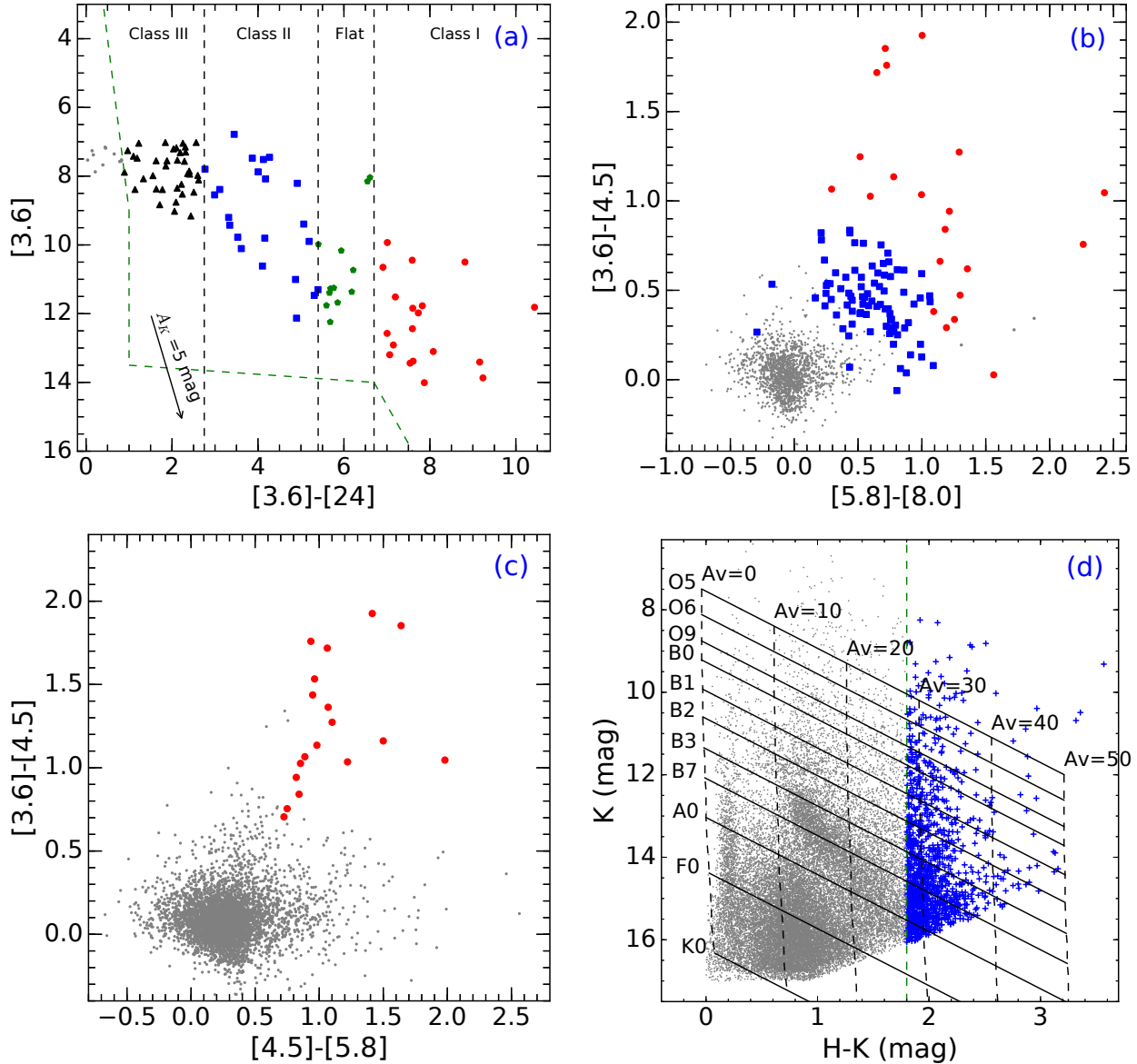


**Figure 7.** YSO selection schemes using the MIR and NIR color-color and color-magnitude criteria. (a) Color-magnitude diagram ( $[3.6]-[24]/[3.6]$ ) of the sources seen toward the N37 region. In the diagram, the selected sources are classified into different classes following the color criteria described in Guieu et al. (2010) and Rebull et al. (2011). Sources at different classes are marked with different symbols: Class I (red circle), Flat spectrum (green pentagon), Class II (blue squares) and Class III (black triangles). An extinction vector for  $A_K = 5$  mag is also shown in the diagram. (b) Color-color diagram ( $[5.8]-[8.0]/[3.6]-[4.5]$ ) of the sources that are detected in all the four *Spitzer*-IRAC bands. The sources are classified after removing possible contaminants based on the classification schemes of Gutermuth et al. (2009) (see text for more details). (c) Color-color diagram ( $[4.5]-[5.8]/[3.6]-[4.5]$ ) of the sources detected in the first three *Spitzer*-IRAC bands (except  $8 \mu\text{m}$ ). The color criteria for this classification were obtained from Hartmann et al. (2005) and Getman et al. (2007). (d) Color-magnitude diagram ( $H-K/K$ ) of all the sources detected in  $H$  and  $K$  bands. A cutoff  $H-K$  color value (i.e. 1.8 mag) was obtained from a nearby reference field ( $15' \times 15'$  area centered at  $l = 25^\circ.372$ ,  $b = 0^\circ.676$ ).

by a green dashed curve, following the criteria given in Guieu et al. (2010). Using this scheme, a total of 19 Class I, 12 Flat-spectrum, 22 Class II, and 36 Class III sources were identified.

2. There are several sources that are not seen in the MIPS GAL  $24 \mu\text{m}$  image, but detected in the *Spitzer*-IRAC/GLIMPSE bands ( $3.6$ ,  $4.5$ ,  $5.8$ , and  $8.0 \mu\text{m}$ ). Hence, the color-color diagram ( $[5.8]-[8.0]/[3.6]-[4.5]$ ) of the sources detected in all four IRAC bands was used to identify the additional YSOs (see Figure 7b). Possible contaminants (such as broad-line active galactic nuclei, PAH-emitting galaxies and shock emission knots) were removed from the sample using the criteria given in

Gutermuth et al. (2009). The selected YSOs were classified into different evolutionary stages using the slopes of the *Spitzer*-IRAC/GLIMPSE spectral energy distribution (SED) (i.e.  $\alpha_{IRAC}$ ) measured from  $3.6$  to  $8.0 \mu\text{m}$  (see Lada et al. 2006, for more details). Finally, using this scheme, we identified a total of 20 Class I and 99 Class II YSOs.

3. Due to prominent nebulosity seen in the IRAC  $8.0 \mu\text{m}$  band, there are several sources that are not detected in the  $8.0 \mu\text{m}$  image, but identified in other three GLIMPSE-IRAC bands ( $3.6$ ,  $4.5$ , and  $5.8 \mu\text{m}$ ). Hence, the color-color diagram ( $[3.6]-[4.5]/[4.5]-[5.8]$ ) was constructed to identify the additional YSOs (see

Figure 7c). The sources that follow  $[4.5]-[5.8] \geq 0.7$  mag and  $[3.6]-[4.5] \geq 0.7$  mag are classified as protostars (Hartmann et al. 2005; Getman et al. 2007). Using this scheme, a total of 17 protostars were identified in the region around the bubble.

4. Presence of circumstellar material makes YSOs to appear much redder than the nearby field stars in the NIR color-magnitude diagram. Hence, we also used NIR color-magnitude diagram ( $H-K/K$ ) to identify additional YSOs toward the N37 region. The  $H-K$  color cut-off of 1.8 was estimated by constructing the color-magnitude diagram ( $H-K/K$ ) of a nearby field region (size  $\sim 15' \times 15'$  area centered at  $l = 25^\circ.372$ ;  $b = 0^\circ.676$ ). This color cut-off differentiate the field stars from the sources having large NIR excess. The NIR color-magnitude diagram of the sources is shown in Figure 7d. Using the NIR scheme, we identified a total of 1203 red sources that could be presumed as YSOs.

There could be overlap of YSOs identified using these four different schemes. In order to have a complete catalog, YSOs identified using different schemes were cross-matched. Finally, a total of 29 Class I, 12 Flat spectrum, 99 Class II, 973 Class III YSOs, and 1066 red sources are identified toward the N37 region.

#### 4.6.2. Surface density analysis of YSOs

In order to examine how the YSOs are clustered in the region around the bubble, a nearest-neighbor (NN) surface density analysis of YSOs was performed following the method given in Schmeja et al. (2008) and Schmeja (2011). Using Monte Carlo simulations, Schmeja et al. (2008) showed that the 20NN surface density is capable to detect clusters with 10–1500 YSOs. Hence, the 20NN surface density analysis of YSOs was performed using a grid size of  $6''.9$  which corresponds to 0.1 pc at a distance of 3 kpc. Figure 8 shows the surface density contours of YSOs overlaid on the *Herschel* 500  $\mu\text{m}$  image. The contour levels are drawn at 15, 18, 22, 27, and 30 YSOs  $\text{pc}^{-2}$ . The positions of all the clumps identified in the *Herschel* column density map are also marked on the image. The YSO clusters are found toward the IRDC, the clump C1 and the pillar-like structure, and many of these YSO clusters are associated with peaks having more than 27 YSOs  $\text{pc}^{-2}$  (see Figure 8). It is already mentioned before that the clump C1 is part of the C25.29+0.31 cloud and is not associated with the N37 molecular cloud. Therefore, the clusters of YSOs located towards the clump C1 might not have any physical association with the N37 bubble.

#### 4.6.3. Spectral Energy Distribution of selected YSOs

In order to infer the physical properties of YSOs (e.g., mass, age), the SED modeling of a few selected YSOs was performed using the SED fitter tool of Robitaille et al. (2006, 2007). The grids of YSO models were computed using the radiation transfer code of Whitney et al. (2003a,b), which assumes an accretion scenario for a pre-main sequence central star, surrounded by a flared accretion disk and a rotationally flattened envelope with cavities. The model grid has 20,000 SED models from Robitaille et al. (2006), estimated using two-dimensional radiative transfer Monte Carlo simulations. Each YSO model gives the output SEDs for 10 inclination angles with masses ranging from 0.1–50  $M_\odot$ . The fitter tool

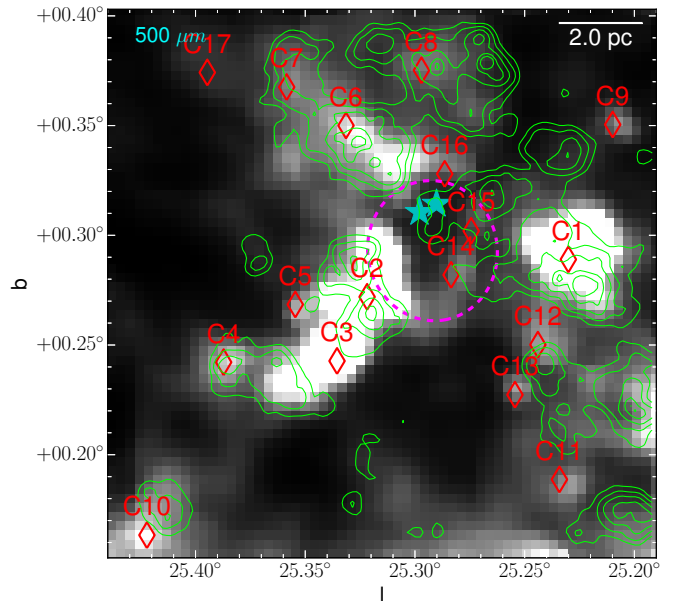


**Figure 8.** Overlay of 20NN surface density contours (green) on the *Herschel* SPIRE 500  $\mu\text{m}$  image. The background 500  $\mu\text{m}$  image is similar to the one shown in Figure 2. The surface density contours of YSOs are drawn at 15, 18, 22, 27, and 30 YSO  $\text{pc}^{-2}$ . The YSOs' clusters are seen toward the pillar, the IRDC, and the clump C1.

tries to find the best possible match of YSO models for the observed multi-wavelength fluxes followed by a chi-square minimization. The distance to the source and interstellar visual extinction ( $A_V$ ) are used as free parameters. We performed the SED modeling of those YSOs that have fluxes at least in five filter bands (among NIR JHK and Spitzer-IRAC bands), in order to constrain the diversity of the modeling parameters. Accordingly, a total of 81 YSOs were selected for the SED fitting. In the models, we used the  $A_V$  in the range from 0–50 mag and the distance ranging from 2–4 kpc. For each YSO, only those models were selected which follow the criterion:  $\chi^2 - \chi_{best}^2 < 3$ , where  $\chi^2$  is taken per data point. Note that the output parameters for each YSO are not unique because several models can satisfy the observed SED. Hence, the weighted mean values were computed for all the model fitted parameters for each YSO. In Table 2, we have listed, the right ascension (J2000), declination (J2000), the weighted mean values of the stellar age, stellar mass, total luminosity, extinction and evolutionary class for a sample of 6 YSOs. The complete table of 81 YSOs is available online in machine readable format.

#### 4.7. Near-infrared H-band polarization

The polarization of background starlight is often used to study the projected plane-of-the-sky magnetic field morphology. The polarization vectors of background stars allow to trace the field direction in the plane of the sky parallel to the direction of polarization (Davis & Greenstein 1951).

NIR polarization data of point sources towards the N37 region were obtained from the GPIPS (see Clemens et al. 2012, for more details) and were covered in several fields i.e., GP0608, GP0609, GP0610, GP0622, GP0623, GP0624, GP0635, GP0636, GP0637, GP0649, GP0650, GP0651. A total of 375 sources with reliable polariza-

**Table 2**  
Physical parameters of selected YSOs derived from the SED modeling.

RA (J2000) (hh:mm:ss)	Dec (J2000) (dd:mm:ss)	Log (Age) (yr)	Mass ( $M_{\odot}$ )	$\log(L_{\text{tot}})$ ( $L_{\odot}$ )	$A_V$ (mag)	Class
18:35:58.8	-06:43:18	$5.52 \pm 0.51$	$2.11 \pm 1.00$	$1.70 \pm 0.16$	$11.49 \pm 4.41$	Class II
18:36:17.7	-06:45:41	$5.55 \pm 0.72$	$1.54 \pm 1.32$	$1.62 \pm 0.24$	$3.74 \pm 2.18$	Class II
18:36:20.0 <sup>C</sup>	-06:44:21	$4.84 \pm 0.55$	$2.17 \pm 1.26$	$1.59 \pm 0.19$	$33.99 \pm 15.19$	Class I
18:36:24.9 <sup>B</sup>	-06:39:41	$6.37 \pm 0.42$	$4.97 \pm 0.91$	$1.81 \pm 0.13$	$3.86 \pm 2.01$	Class II
18:36:25.5 <sup>B</sup>	-06:39:46	$5.48 \pm 0.60$	$3.94 \pm 0.91$	$1.53 \pm 0.28$	$0.73 \pm 1.12$	Class I
18:36:36.1 <sup>P</sup>	-06:37:51	$5.64 \pm 0.43$	$2.22 \pm 0.98$	$1.66 \pm 0.20$	$2.63 \pm 1.50$	Class II

<sup>B</sup> YSOs located toward the N37 bubble

<sup>C</sup> YSOs located toward C1

<sup>P</sup> YSOs located toward the pillar

tion measurements were identified in the  $15' \times 15'$  area towards the N37 region using the criteria of  $P/\sigma_P \geq 2.5$  and UF of 1. In Figure 9a, we show a color-color diagram ( $H - K$  vs.  $J - H$ ) of the selected sources and find that the majority of the sources are either reddened giants or main-sequence stars. Hence, it is evident from the NIR color-color diagram that the majority of stars are located behind the N37 molecular cloud. The histograms of the degree of polarization and the corresponding Galactic position angles are also shown in Figures 9b and 9c, respectively, which show that the majority of the sources have degree of polarization and position angle of about 1.5% and  $\sim 60^\circ$ , respectively. If it is considered that the dust components responsible to polarize the background starlight are aligned along the magnetic field lines, then the corresponding plane-of-sky component of the magnetic field is oriented at a position angle of  $\sim 60^\circ$ .

The polarization vectors overlaid on the velocity integrated  $^{13}\text{CO}$  map are shown in Figure 10a. To examine the average distribution of NIR  $H$ -band polarization, the mean degree of polarization vectors superimposed on the *Spitzer*  $8 \mu\text{m}$  image are shown in Figure 10b. In order to study the mean polarization, our selected  $15' \times 15'$  spatial area was divided into 225 grids having  $1' \times 1'$  area for each grid and the mean polarization value for each grid is computed using the average Q and U Stokes parameters of all the  $H$ -band sources located inside that particular grid. Using the  $H$ -band polarization data, one cannot trace the morphology of the plane-of-the-sky projection of the magnetic field toward the dense clumps, where extinction is generally high enough for a background source to be detected in the NIR  $H$ -band.

#### 4.8. Distribution and kinematics of molecular gas

The GRS  $^{13}\text{CO}$  ( $J=1-0$ ) line data were utilized to examine the distribution and kinematics of the molecular gas towards the N37 bubble. Additionally, the velocity information of gas inferred from the  $^{13}\text{CO}$  data is used to know the physical association of different subregions seen in the selected region around the bubble. The integrated GRS  $^{13}\text{CO}$  ( $J=1-0$ ) velocity channel maps (at intervals of  $1 \text{ km s}^{-1}$ ) are shown in Figure 11, tracing different subregions along the line of sight. As mentioned before from the  $^{13}\text{CO}$  profile that the molecular cloud associated with the bubble N37 (i.e., N37 molecular cloud) is depicted in the velocity range from  $37-43 \text{ km s}^{-1}$ . In this velocity range, three condensations (see last panel of Figure 11 for C2, C3, and C4) located towards the pillar-like structure are well detected in the channel maps. The in-

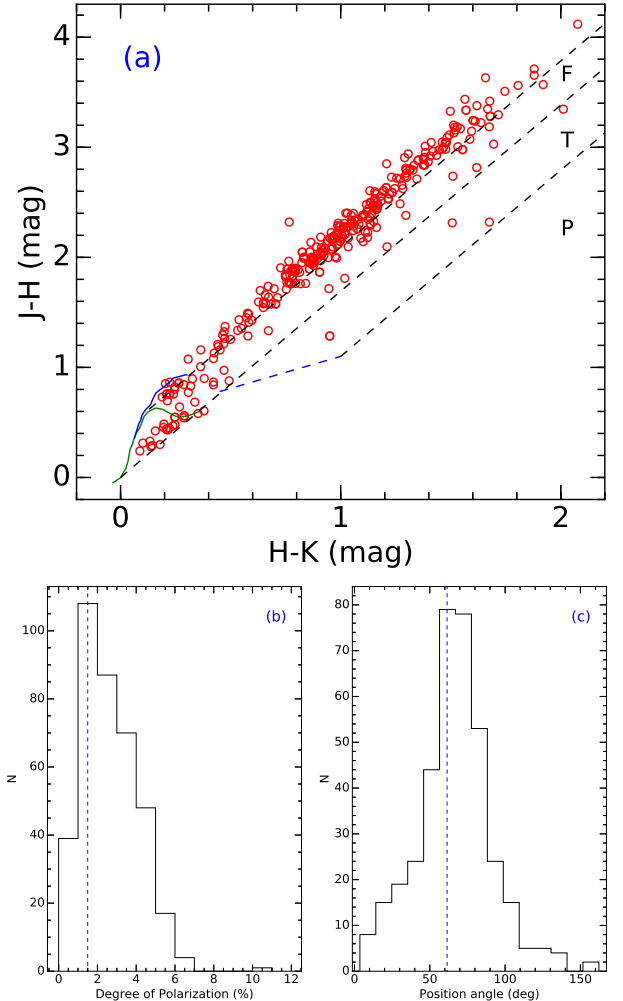


**Figure 9.** (a) NIR color-color diagram ( $J-H/H-K$ ) of the GPIPS sources with  $P/\sigma_P \geq 2.5$ . The solid green and blue curves are the unreddened loci of main-sequence dwarf stars and giants (from Bessell & Brett 1988) respectively. The blue dashed line shows the locus of Classical T Tauri (CTTS) obtained from Meyer et al. (1997). Three parallel black dashed lines are the reddening vectors drawn from the base of the main-sequence locus, from the turning point of the main-sequence locus, and from the tip of the CTTS locus, using the reddening laws from Cohen et al. (1981). The sources in the ‘F’ region are generally evolved field stars, while the sources in the ‘T’ region are mainly Class II YSOs, and the sources in the ‘P’ region are considered as Class I YSOs (see Ojha et al. 2004, for more details). The color-color diagram implies that sources with  $P/\sigma_P \geq 2.5$  are mainly reddened background main-sequence and giant stars. (b) Histogram of the degree of polarizations and (c) histogram of the Galactic position angles of all the sources with  $P/\sigma_P \geq 2.5$  toward the N37 region.

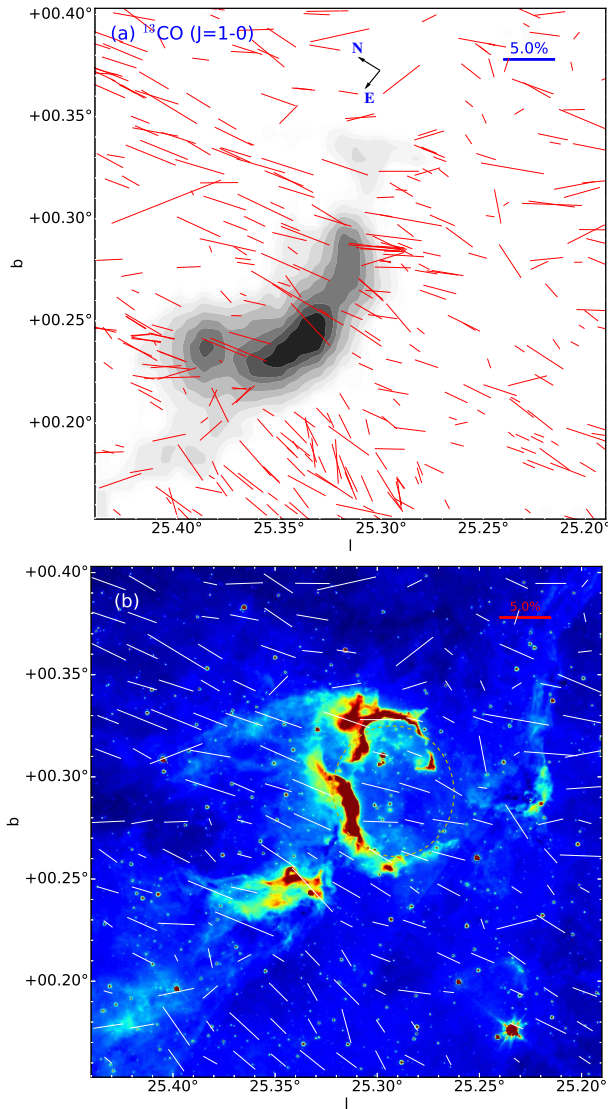


**Figure 10.** (a) NIR  $H$ -band polarization vectors (red lines) of all the sources with  $P/\sigma_P \geq 2.5$ , overplotted on the velocity integrated  $^{13}\text{CO}$  map. (b) Mean  $H$ -band polarization vectors (for a grid size of  $1' \times 1'$ ) overplotted on the *Spitzer*  $8\ \mu\text{m}$  image.

egrated GRS  $^{13}\text{CO}$  intensity map for the C25.29+0.31<sup>2</sup> was previously reported by Anderson et al. (2009) having  $V_{LSR}$  of  $\sim 45.9\ \text{km s}^{-1}$  with a velocity range of  $\sim 43\text{--}48\ \text{km s}^{-1}$ . Based on the CO velocity profile and channel maps (Figure 11), we infer that two nearby but distinct molecular clouds (i.e. N37 molecular cloud and C25.29+0.31) are present in our selected area of analysis. Hence, there could be a possibility for physical interaction between these two nearby molecular clouds.

Note that the position-velocity analysis of these clouds is not yet explored. Figure 12a shows an integrated velocity map ( $37\text{--}43\ \text{km s}^{-1}$ ) of the region around the bubble N37, which reveals the physical association of molecular condensations with the N37 molecular cloud. In general, the position-velocity plots of the molecular gas are often used to search for any expansion of gas and/or outflow activity within a given cloud (e.g., Arce et al.

2011; Dewangan et al. 2016). The position-velocity diagrams of  $^{13}\text{CO}$  gas associated with the N37 cloud are shown in Figures 12c and 12e. The positions of the massive OB stars and the condensations are also marked in the position-velocity diagrams. The velocity gradients are evident toward the condensations C2, C3, and C4, which can be indicative of the outflow activities within each of them. Note that the angular resolution of the  $^{13}\text{CO}$  data ( $45''$ ) is coarse therefore we cannot further explore the outflow activity within these condensations. Additionally, an inverted C-like structure appears in Figure 12c (follow the marked curve) and the massive OB stars are located near the center of the structure. Such structure is indicative of an expanding shell associated with the H II region in the bubble N37 (e.g., Arce et al. 2011; Dewangan et al. 2016). The study of  $^{13}\text{CO}$  line data suggests the presence of molecular outflow(s) and the expanding H II region with an expansion velocity of  $\sim 2.5\ \text{km s}^{-1}$ . This expansion velocity corresponds to the half of the velocity range for the inverted C-like structure seen in the position-velocity diagram.

The integrated velocity map for a larger velocity range ( $37\text{--}48\ \text{km s}^{-1}$ ), which covers both the N37 and C25.29+0.31 molecular clouds, is presented in Figure 12b. We have also constructed the position-velocity diagrams of  $^{13}\text{CO}$  gas in the corresponding velocity range (see Figures 12d and 12f). In Figures 12d and 12f, we find that the red-shifted component ( $43\text{--}48\ \text{km s}^{-1}$ ) and the blue-shifted component ( $37\text{--}43\ \text{km s}^{-1}$ ) are well separated by a lower intensity intermediated velocity emission, which is referred as a broad bridge feature. This feature in the position-velocity diagram is generally seen at the interface of the colliding molecular clouds (see Haworth et al. 2015a,b, for more detail). The implication of this feature is presented in the discussion section (Section 5).

## 5. DISCUSSION

As mentioned before, there are two molecular clouds (i.e. N37 molecular cloud and C25.29+0.31) present in the region around the bubble. The position-velocity analysis of the molecular gas towards these clouds reveals a broad bridge-like feature. This bridge-like feature is indicative of a cloud-cloud collision (Fukui et al. 2014; Haworth et al. 2015a,b; Torii et al. 2015). These authors also suggested that the collision between two molecular clouds can be a potential mechanism to trigger the formation of massive stars. Very recently, observational evidences of the cloud-cloud collision and the formation of massive stars through this process have been reported in the Galactic star-forming regions RCW120 (Torii et al. 2015) and RCW 38 (Fukui et al. 2016).

According to Habe & Ohta (1992) and Torii et al. (2015), a collision between two non-identical clouds can produce a dense layer at the interface of these clouds and can create a cavity in the large cloud (see Figure 12 of Torii et al. 2015). The compressed dense layer has the ability to develop the dense cores, which can subsequently form massive stars. After the formation of massive stars, their strong UV radiation can ionize the surrounding gas and develop an H II region. Torii et al. (2015) suggested that the cloud-cloud collision has formed an O-type star in the RCW 120 re-

<sup>2</sup> [http://www.bu.edu/iar/files/script-files/research/hii\\_regions/region\\_pages/C25.29+0.31.html](http://www.bu.edu/iar/files/script-files/research/hii_regions/region_pages/C25.29+0.31.html)

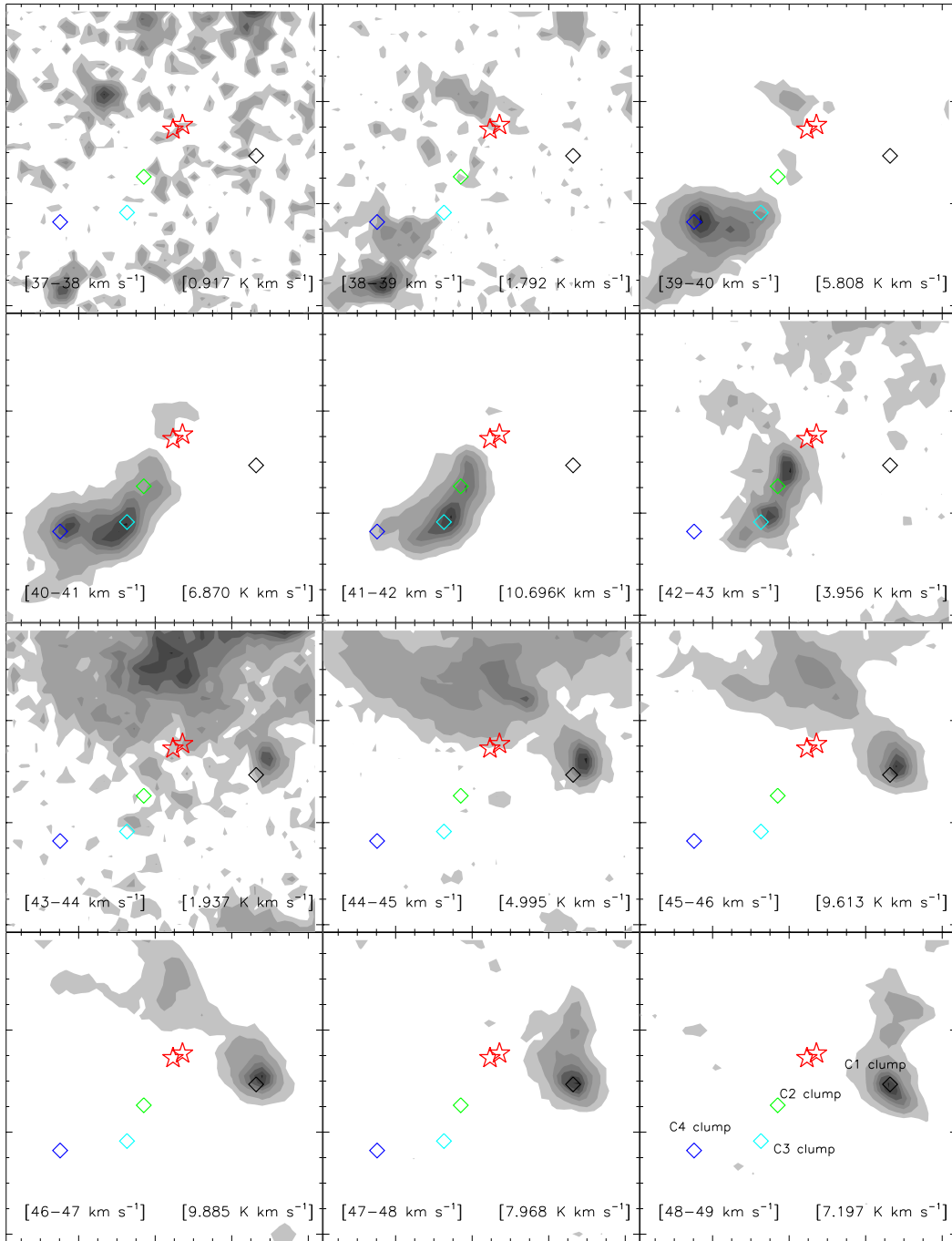


**Figure 11.** The  $^{13}\text{CO}(J=1-0)$  velocity channel contour maps of the N37 region. The velocity range (in  $\text{km s}^{-1}$ ) is indicated in the bottom left corner of each panel. The contours are drawn at 10, 20, 40, 55, 70, 85 and 98% of the peak value, which is also written in the bottom right corner of each panel. Other marked symbols and labels are same as Figures 3 and 6.

gion, and made it to appear as a broken bubble. It is mentioned before that the N37 molecular cloud hosts a pillar-like structure, IRDC, and the MIR bubble N37. The cloud also harbors YSOs clusters that are associated with the IRDC and pillar-like structure. It is possible that the cloud-cloud collision has influenced the star formation within the N37 molecular cloud (including the IRDC, OB stars, and the pillar-like structure). The massive OB stars might have formed due to a similar formation mechanism as it is reported for RCW 120. With time, the massive OB stars developed an H II region and the MIR bubble morphology appears to be originated

due to the expansion of the photoionized gas (see Section 4.4). It is also possible that the collision between two molecular clouds might have developed the broken cavity and that is why the N37 bubble has appeared with a broken structure. However, we do not have enough observational evidences to firmly conclude about the origin of the broken feature of the N37 bubble.

We calculated the dynamical age of the H II region ( $t_{dyn}$ ) towards the N37 bubble to be  $\approx 0.7$  Myr for an ambient density of  $10000 \text{ cm}^{-3}$  (see Section 4.3). In general, the average ages of Class I and Class II YSOs are  $\sim 0.44$  Myr and  $\sim 1-3$  Myr (Evans et al. 2009), respec-

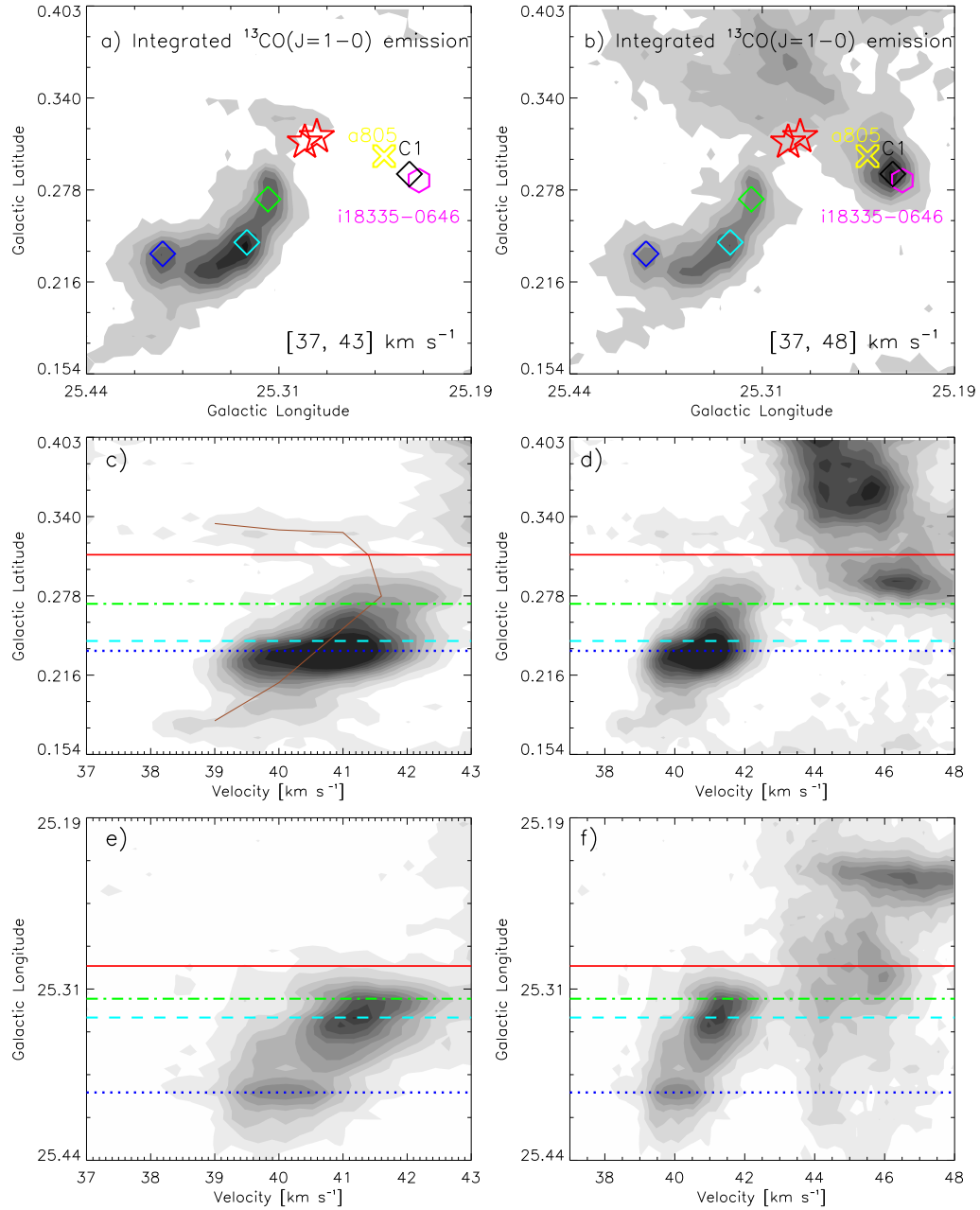


**Figure 12.** The distribution of molecular gas toward the N37 molecular cloud and the cloud associated with IRAS 18335–0646/C1 clump. a) A contour map of integrated  $^{13}\text{CO}$  emission in the velocity range of 37 to 43  $\text{km s}^{-1}$ . b) A contour map of integrated  $^{13}\text{CO}$  emission in the velocity range of 37 to 48  $\text{km s}^{-1}$ . In the top two panels, four largest condensations seen in the *Herschel* column density map are also marked by diamond symbols. The positions of IRAS 18335–0646 (hexagon) and an O7II type source (a805; marked by an X symbol) are also highlighted in the top two panels. c) Latitude-velocity map of  $^{13}\text{CO}$  in the velocity range of 37 to 43  $\text{km s}^{-1}$ . An inverted C-like structure is evident and is marked by a brown curve. d) Latitude-velocity map of  $^{13}\text{CO}$  in the velocity range of 37 to 48  $\text{km s}^{-1}$ . e) Longitude-velocity map of  $^{13}\text{CO}$  in the velocity range of 37 to 43  $\text{km s}^{-1}$ . f) Longitude-velocity map of  $^{13}\text{CO}$  in the velocity range of 37 to 48  $\text{km s}^{-1}$ . The molecular cloud associated with the bubble is traced in the velocity range of 37 to 43  $\text{km s}^{-1}$ . The cloud associated with the IRAS 18335–0646/C1 clump is depicted in the velocity range of 43 to 48  $\text{km s}^{-1}$ . The position-velocity diagram suggests the possibility of interaction between the N37 molecular cloud and the cloud associated with the C1 clump region (see text for more details). In all the position-velocity plots, the positions of ionizing star and condensations (associated with the N37 cloud) are shown by broken lines.

tively. Considering these ages, it is unlikely that the star formation in the N37 cloud has been triggered by the expansion of the H II region. For further confirmation, we determined the average ages of YSOs toward the bubble, the pillar and the clump C1 which is, however, part of C25.29+0.31 molecular cloud. The distribution of Class I and Class II YSOs overplotted on the  $8\ \mu\text{m}$  image are shown in Figure 13a. A total of 13, 7 and 10 YSOs are found to be situated toward the N37 bubble, the pillar and the C1, respectively, for which the SED modeling was performed (see Figure 13b). Corresponding mean ages of these YSOs are estimated to be 1.0, 0.7 and 0.7 Myr, respectively, which are comparable to the dynamical age of the H II region of 0.7 Myr. For a triggered star formation to occur the mean ages of YSOs should be less compared to the dynamical age of the H II region. However, the mean ages are associated with large standard deviations ( $\sim 0.5$  Myr) and hence, it is not possible to make a definite conclusion from this analysis.

We have also plotted the cumulative distribution of ages of YSOs toward the bubble, C1, and the pillar (see Figure 13c). It can be seen in the cumulative distributions of the ages that the majority of the YSOs (at least  $\sim 60\%$ ) located towards the pillar are younger than the YSOs towards the bubble and C1. Hence, the formation of stars towards the pillar and C1 might have started later than the bubble. Though the YSOs associated with the pillar and the C1 are younger than the YSOs towards the bubble, the dynamical age of the H II region is not consistent enough to conclude whether they have formed due to the influence of bubble/massive OB stars. Note that in this paper we do not discuss results related to the C25.29+0.31 cloud, which hosts the clump C1, the IRAS 18335–0646, and the star a805 (an O7II spectral type) (see Marco & Negueruela 2011). It should be mentioned here that the pillars are generally assumed to be potential sights of triggered star formation (Klein et al. 1980; Elmegreen 2011), and young stars are expected to appear at the tip of the pillars (Hester & Desch 2005). A few Class I and Class II YSOs are found to be associated with the pillar (see Figure 13a) and these YSOs might have formed by some other mechanisms than triggered by the OB stars or H II region.

It can be noticed in Figure 10b, even though the mean polarization position angles are generally uniform at a Galactic position angle of  $\sim 60^\circ$  throughout the region, random changes in the polarization position angles are noticed near the interface of the N37 molecular cloud and the clump C1 which is part of the C25.29+0.31 molecular cloud. We suggest that this change in the polarization position angles can be explained by a distortion of gas due to the collision between these two molecular clouds.

Overall, this region correlates well with the observational signatures proposed for the cloud-cloud collision process. In addition to the formation of OB stars, the cloud-cloud collision might have also triggered the formation of several other YSO clusters in the N37 molecular cloud.

## 6. CONCLUSIONS

We performed a multi-wavelength analysis of the Galactic MIR bubble N37 and its surrounding environment. The aim of this study is to investigate the physical environment and star formation mechanisms around the

bubble. The main conclusions of this study are the following.

1. In the selected  $15' \times 15'$  region around the MIR bubble N37, two molecular clouds (N37 molecular cloud and C25.29+0.31) are present along the line of sight. The molecular cloud associated with the bubble (i.e. N37 molecular cloud) is depicted in the velocity range from 37 to 43  $\text{km s}^{-1}$ , while the C25.29+0.31 cloud is traced in the velocity range from 43 to 48  $\text{km s}^{-1}$ . The N37 molecular cloud appears to be blue-shifted with respect to the C25.29+0.31 cloud.

2. Using photometric criteria, we find a total of seven OB stars within the N37 bubble, and spectroscopically confirmed two of these sources as O9V and B0V stars. The physical association of these sources with the N37 bubble is also confirmed by estimating their spectro-photometric distances. The O9V star is found as the primary ionizing source of the region. This result is in agreement with the Lyman continuum flux analysis using the 20 cm data.

3. Several molecular condensations surrounding the N37 bubble are identified in the *Herschel* column density map. The physical association of these condensations with the N37 bubble is inferred using the molecular gas distribution as traced in the integrated  $^{13}\text{CO}$  ( $J=1-0$ ) map. Surface density analysis of the identified YSOs reveals that the YSOs are clustered toward these molecular condensations.

4. The mean ages of YSOs located in different parts of the region indicate that it is unlikely that these YSOs are triggered by energetics of the OB stars present within the bubble. This interpretation is supported with the knowledge of the dynamical age of the H II region.

5. The position-velocity analysis of  $^{13}\text{CO}$  data shows that two clouds (N37 molecular cloud and C25.29+0.31) are interconnected with a lower intensity emission known as broad bridge structure. The presence of such feature suggests the possibility of interaction between the N37 molecular cloud and the C25.29+0.31 cloud.

6. The position-velocity analysis of  $^{13}\text{CO}$  emission also reveals an inverted C-like structure, suggesting the signature of an expanding H II region. Based on the pressure calculations ( $P_{\text{HII}}$ ,  $P_{\text{rad}}$ , and  $P_{\text{wind}}$ ), the photoionized gas associated with the bubble is found as the primary contributor for the feedback mechanism in the N37 cloud. Possibly the expanding H II region is responsible for the origin of the MIR bubble N37.

7. The collision between two clouds (i.e. N37 molecular cloud and C25.29+0.31) might have changed the uniformity of the molecular cloud which is depicted by a slight change in the polarization position angles of background starlight.

8. The collision between the N37 molecular cloud and the C25.29+0.31 cloud might have triggered the formation of massive OB stars. This process might also have triggered the formation of YSOs clusters in the N37 molecular cloud.

We thank the anonymous referee for the constructive comments. We are also grateful to Dr. A. Luna for providing the IDL-based program for the analysis of CO line data. We thank the staff of IAO, Hanle and CREST, Hosakote, that made the observations using HCT possi-

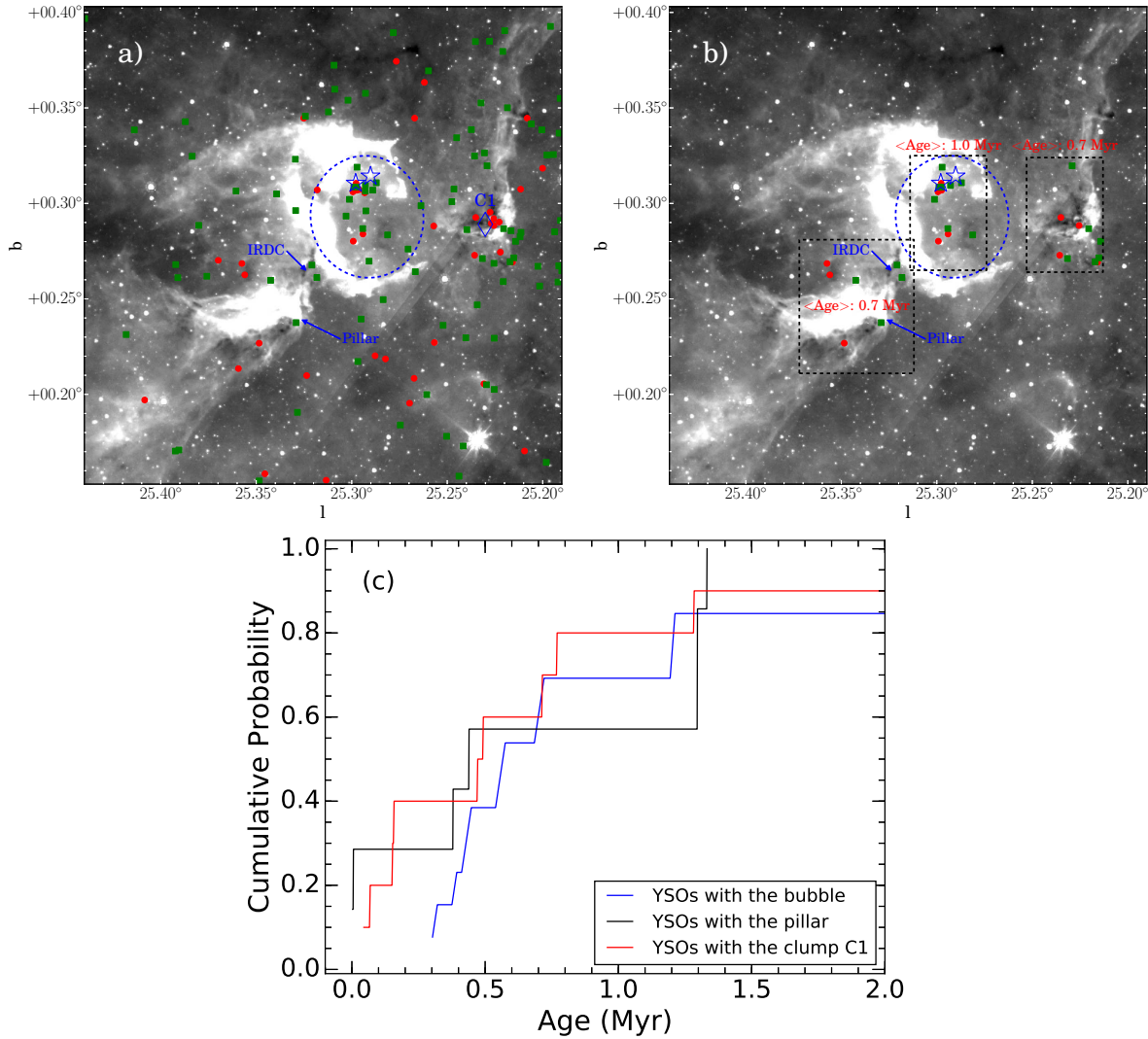


**Figure 13.** (a) Class I (red circles) and Class II (green squares) YSOs are overlotted on the *Spitzer*-IRAC 8  $\mu\text{m}$  image of the N37 region. Other symbols are same as in Figure 1. Some Class I YSOs are located inside the bubble and are also associated with C1 clump. A few Class I/II YSOs are also detected toward the pillar. (b) The positions of selected YSOs (in the N37 bubble, C1 clump, and pillars regions; see black dotted rectangles), for which the SED analysis was performed (see text for more details). In each selected region, the average age of YSOs is also shown. (c) Cumulative distributions of ages of YSOs toward the bubble, the pillar and the clump C1 are shown by blue, black and red lines, respectively.

ble. The facilities at IAO and CREST are operated by the Indian Institute of Astrophysics, Bangalore. We acknowledge the use of the AAVSO Photometric All-Sky Survey (APASS), funded by the Robert Martin Ayers Sciences Fund. This work is based on data obtained as part of the UKIRT Infrared Deep Sky Survey. This publication made use of data products from the Two Micron All Sky Survey (a joint project of the University of Massachusetts and the Infrared Processing and Analysis Center/ California Institute of Technology, funded by NASA and NSF), archival data obtained with the *Spitzer* Space Telescope (operated by the Jet Propulsion Laboratory, California Institute of Technology under a contract with NASA). This publication makes use of molecular line data from the Boston University-FCRAO Galactic Ring Survey (GRS). The GRS is a joint project of Boston University and Five College Radio Astronomy Observatory, funded by the National Science Foundation (NSF) under grants AST-9800334, AST-0098562, and AST-0100793. This publication makes use of the Galactic Plane Infrared Polarization Survey (GPIPS). The GPIPS was

conducted using the *Mimir* instrument, jointly developed at Boston University and Lowell Observatory and supported by NASA, NSF, and the W.M. Keck Foundation. LKD is supported by the Department of Space, Government of India.

#### REFERENCES

- Aguirre, J. E., Ginsburg, A. G., Dunham, M. K., et al. 2011, *ApJS*, 192, 4  
 Anderson, L. D., Bania, T. M., Jackson, J. M., et al. 2009, *ApJS*, 181, 255  
 Arce, H. G., Borkin, M. A., Goodman, A. A., Pineda, J. E., & Beaumont, C. N. 2011, *ApJ*, 742, 105  
 Battersby, C., Bally, J., Ginsburg, A., et al. 2011, *A&A*, 535, A128  
 Beaumont, C. N., & Williams, J. P. 2010, *ApJ*, 709, 791  
 Benjamin, R. A., Churchwell, E., Babler, B. L., et al. 2003, *PASP*, 115, 953  
 Bessell, M. S., & Brett, J. M. 1988, *PASP*, 100, 1134  
 Bisbas, T. G., Wünsch, R., Whitworth, A. P., & Hubber, D. A. 2009, *A&A*, 497, 649  
 Blitz, L., Fich, M., & Stark, A. A. 1982, *ApJS*, 49, 183

- Bohlin, R. C., Savage, B. D., & Drake, J. F. 1978, *ApJ*, 224, 132
- Bressert, E., Ginsburg, A., Bally, J., et al. 2012, *ApJ*, 758, L28
- Carey, S. J., Noriega-Crespo, A., Price, S. D., et al. 2005, *Bulletin of the American Astronomical Society*, 37, 63.33
- Casali, M., Adamson, A., Alves de Oliveira, C., et al. 2007, *A&A*, 467, 777
- Churchwell, E., Povich, M. S., Allen, D., et al. 2006, *ApJ*, 649, 759
- Churchwell, E., Watson, D. F., Povich, M. S., et al. 2007, *ApJ*, 670, 428
- Clemens, D. P., Pinnick, A. F., Pavel, M. D., & Taylor, B. W. 2012, *ApJS*, 200, 19
- Cohen, J. G., Persson, S. E., Elias, J. H., & Frogel, J. A. 1981, *ApJ*, 249, 481
- Dale, J. E. 2015, *New A Rev.*, 68, 1
- Davis, L., Jr., & Greenstein, J. L. 1951, *ApJ*, 114, 206
- Deharveng, L., Schuller, F., Anderson, L. D., et al. 2010, *A&A*, 523, A6
- Dewangan, L. K., Ojha, D. K., Anandarao, B. G., Ghosh, S. K., & Chakraborti, S. 2012, *ApJ*, 756, 151
- Dewangan, L. K., & Ojha, D. K. 2013, *MNRAS*, 429, 1386
- Dewangan, L. K., Luna, A., Ojha, D. K., et al. 2015, *ApJ*, 811, 79
- Dewangan, L. K., Baug, T., Ojha, D. K., et al. 2016, *ApJ*, 826, 27
- Elmegreen, B. G. 1998, in *ASP Conf. Ser.* 148, *Origins*, ed. C. E. Woodward, J. M. Shull, & H. A. Thronson, Jr. (San Francisco, CA: ASP), 150
- Elmegreen, B. G. 2011, *EAS Publications Series*, 51, 45
- Evans, N. J., II, Dunham, M. M., Jørgensen, J. K., et al. 2009, *ApJS*, 181, 321
- Froebrich, D., Davis, C. J., Ioannidis, G., et al. 2011, *MNRAS*, 413, 480
- Fukui, Y., Ohama, A., Hanaoka, N., et al. 2014, *ApJ*, 780, 36
- Fukui, Y., Torii, K., Ohama, A., et al. 2016, *ApJ*, 820, 26
- Furukawa, N., Dawson, J. R., Ohama, A., et al. 2009, *ApJ*, 696, L115
- Getman, K. V., Feigelson, E. D., Garmire, G., Broos, P., & Wang, J. 2007, *ApJ*, 654, 316
- Griffin, M. J., Abergel, A., Abreu, A, et al. 2010, *A&A*, 518L, 3
- Guieu, S., Rebull, L. M., Stauffer, J. R., et al. 2010, *ApJ*, 720, 46
- Gutermuth, R. A., Megeath, S. T., Myers, P. C., et al. 2009, *ApJS*, 184, 18
- Gutermuth, R. A., & Heyer, M. 2015, *AJ*, 149, 64
- Habe, A., & Ohta, K. 1992, *PASJ*, 44, 203
- Hartmann, L., Megeath, S. T., Allen, L., et al. 2005, *ApJ*, 629, 881
- Haworth, T. J., Tasker, E. J., Fukui, Y., et al. 2015a, *MNRAS*, 450, 10
- Haworth, T. J., Shima, K., Tasker, E. J., et al. 2015b, *MNRAS*, 454, 1634
- Helfand, D. J., Becker, R. H., White, R. L., Fallon, A., & Tuttle, S. 2006, *AJ*, 131, 2525
- Hester, J. J., & Desch, S. J. 2005, *Chondrites and the Protoplanetary Disk*, 341, 107
- Hildebrand, R. H. 1983, *QJRAS*, 24, 267
- Hou, L. G., & Han, J. L. 2014, *A&A*, 569, 125
- Indebetouw, R., Mathis, J. S., Babler, B. L., et al. 2005, *ApJ*, 619, 931
- Jackson, J. M., Rathborne, J. M., Shah, R. Y., et al. 2006, *ApJS*, 163, 145
- Klein, R. I., Sandford, M. T., & Whitaker, R. W. 1980, *BAAS*, 12, 821
- Kuiper, R., Yorke, H. W., & Turner, N. J. 2015, *ApJ*, 800, 86
- Kurtz S., 2002, *ASPC*, 267, 81
- Lada, C. J., Muench, A. A., Luhman, K. L., et al. 2006, *AJ*, 131, 1574
- Lang, K. R. 1999, *Astrophysical formulae / K.R. Lang*. New York : Springer, 1999. (Astronomy and astrophysics library, ISSN0941-7834),
- Launhardt, R., Stutz, A. M., Schmiedeke, A., et al. 2013, *A&A*, 551, A98
- Lawrence, A., Warren, S. J., Almaini, O., et al. 2007, *MNRAS*, 379, 1599
- Lucas, P. W., Hoare, M. G., Longmore, A., et al. 2008, *MNRAS*, 391, 136
- Mallick, K. K., Ojha, D. K., Tamura, M., et al. 2015, *MNRAS*, 447, 2307
- Marco, A. & Negueruela, I. 2011, *A&A*, 534, 114
- Martins, F., & Plez, B. 2006, *A&A*, 457, 637
- Meyer, M. R., Calvet, N., & Hillenbrand, L. A. 1997, *AJ*, 114, 288
- Moran, J. M. 1983, *Rev. Mexicana Astron. Astrofis.*, 7, 95
- Muijres, L. E., Vink, J. S., de Koter, A., Müller, P. E., & Langer, N. 2012, *A&A*, 537, A37
- Nielbock, M., Launhardt, R., Steinacker, J., et al. 2012, *A&A*, 547, A11
- Ninan, J. P., Ojha, D. K., Ghosh, S. K., et al. 2014, *Journal of Astronomical Instrumentation*, 3, 1450006
- Ohama, A., Dawson, J. R., Furukawa, N., et al. 2010, *ApJ*, 709, 975
- Ojha, D. K., Ghosh, S. K., Kulkarni, V. K., et al. 2004, *A&A*, 415, 1039
- Oskinova, L. M., Todt, H., Ignace, R., et al. 2011, *MNRAS*, 416, 1456
- Pandey, A. K., Upadhyay, K., Nakada, Y., & Ogura, K. 2003, *A&A*, 397, 191
- Pecaut, M. J., & Mamajek, E. E. 2013, *ApJS*, 208, 9
- Peretto, N. & Fuller, G.A. 2009, *A&A*, 505, 405
- Peters, T., Klaassen, P. D., Mac Low, M.-M., Klessen, R. S., & Banerjee, R. 2012, *ApJ*, 760, 91
- Pickles, A. J. 1998, *PASP*, 110, 863
- Poglitsch, A., Waelkens, C., Geis, N., et al. 2010, *A&A*, 518, L2
- Povich, M. S., Stone, J. M., Churchwell, E., et al. 2007, *ApJ*, 660, 346
- Rebull, L. M., Johnson, C. H., Hoette, V., et al. 2011, *AJ*, 142, 25
- Robitaille, T. P., Whitney, B. A., Indebetouw, R., Wood, K., & Denzmore, P. 2006, *ApJS*, 167, 256
- Robitaille, T. P., Whitney, B. A., Indebetouw, R., & Wood, K. 2007, *ApJS*, 169, 328
- Sadavoy, S. I., di Francesco, J., André, P., et al. 2012, *A&A*, 540, A10
- Schmeja, S., Kumar, M. S. N., & Ferreira, B. 2008, *MNRAS*, 389, 1209
- Schmeja, S. 2011, *Astronomische Nachrichten*, 332, 172
- Schuller, F., Menten, K. M., Contreras, Y., et al. 2009, *A&A*, 504, 415
- Shirley, Y. L., Ellsworth-bowers, T. P., Svoboda, B., et al. 2013, *ApJS*, 209, 2
- Simpson, R. J., Povich, M. S., Kendrew, S., et al. 2012, *MNRAS*, 424, 2442
- Skrutskie, M. F., Cutri, R. M., Stiening, R., et al. 2006, *AJ*, 131, 1163
- Smith, L. J., Norris, R. P. F., & Crowther, P. A. 2002, *MNRAS*, 337, 1309
- Spitzer, L. 1978, *Physical processes in the interstellar medium*, by Lyman Spitzer. New York Wiley-Interscience, 1978. 333 p.
- Stahler, S. W., & Palla, F. 2005, *The Formation of Stars*, by Steven W. Stahler, Francesco Palla, pp. 865. ISBN 3-527-40559-3. Wiley-VCH, January 2005., 865
- Strömgren B., 1939, *ApJ*, 89, 526
- Tan, J. C., Beltrán, M. T., Caselli, P., et al. 2014, *Protostars and Planets VI*, 149
- Torii, K., Hasegawa, K., Hattori, Y., et al. 2015, *ApJ*, 806, 7
- Walborn, N. R., & Fitzpatrick, E. L. 1990, *PASP*, 102, 379
- Watson, C., Hanspal, U., & Mengistu, A. 2010, *ApJ*, 716, 1478
- Wegner, W. 1994, *MNRAS*, 270, 229
- Whitney, B. A., Wood, K., Bjorkman, J. E., & Cohen, M. 2003a, *ApJ*, 598, 1079
- Whitney, B. A., Wood, K., Bjorkman, J. E., & Wolff, M. J. 2003b, *ApJ*, 591, 1049
- Wienen, M., Wyrowski, F., Schuller, F., et al. 2012, *A&A*, 544, 146
- Williams, J. P., de Geus, E. J., & Blitz, L. 1994, *ApJ*, 428, 693
- Zinnecker, H., & Yorke, H. W. 2007, *ARA&A*, 45, 481